

# Display Supersampling

NIRANJAN DAMERA-VENKATA and NELSON L. CHANG

Hewlett-Packard Laboratories

Supersampling is widely used by graphics hardware to render anti-aliased images. In conventional supersampling, multiple scene samples are computationally combined to produce a single screen pixel. We consider a novel imaging paradigm that we call *display supersampling*, where multiple display samples are physically combined via the superimposition of multiple image subframes. Conventional anti-aliasing and texture mapping techniques are shown inadequate for the task of rendering high-quality images on supersampled displays. Instead of requiring anti-aliasing filters, supersampled displays actually require alias generation filters to cancel the aliasing introduced by nonuniform sampling. We present fundamental theory and efficient algorithms for the real-time rendering of high-resolution anti-aliased images on supersampled displays. We show that significant image quality gains are achievable by taking advantage of display supersampling. We prove that alias-free resolution beyond the Nyquist limits of a single subframe may be achieved by designing a bank of alias-canceling rendering filters. In addition, we derive a practical noniterative filter bank approach to real-time rendering and discuss implementations on commodity graphics hardware.

Categories and Subject Descriptors: I.3.3 [Computer Graphics]: Picture/Image Generation—Antialiasing; display algorithms; I.4.0 [Image Processing and Computer Vision]: General—Image displays

General Terms: Algorithms, Theory, Design

Additional Key Words and Phrases: Image display, anti-aliasing, supersampling, super-resolution, nonuniform sampling, multiprojector displays, superimposed projection

## ACM Reference Format:

Damera-Venkata, N. and Chang, N. L. 2009. Display supersampling. ACM Trans. Graph. 28, 1, Article 9 (January 2009), 19 pages. DOI = 10.1145/1477926.1477935 <http://doi.acm.org/10.1145/1477926.1477935>

## 1. INTRODUCTION

Supersampling is a widely used technique in computer graphics for anti-aliased rendering [Akenine-Möller and Haines 2002]. In supersampling, multiple scene samples, taken at different locations with respect to a screen pixel, are computationally combined via filtering to produce an anti-aliased image at the scene resolution. This step is often accomplished by computationally combining multiple images rendered at subpixel offsets [Fuchs et al. 1985; Haeberli and Akeley 1990].

There has, however, been little investigation of the closely related supersampling problem for displays where an image is formed by physically combining multiple superimposed display images. We refer to this novel imaging paradigm as *display supersampling*, or DSS. One example of DSS is the superimposition of the light output from multiple projectors (or superimposed projection). Another example is a jittered light modulator that is capable of precise image shifting [Allen and Ulichney 2005]. Such a paradigm has wide reaching implications, since it may be far more practical to combine multiple lower-resolution display devices than to construct a single higher-resolution device to achieve similar image quality.

Given a high-resolution image to be displayed, the rendering task in DSS is to compute subframe images that, when superimposed,

produce a high-quality reproduction of the given image. This article develops fundamental theory and efficient real-time algorithms for the optimal rendering of high-resolution anti-aliased images on supersampled displays. We show both theoretically and via simulation that anti-aliased rendering on supersampled displays allows for significantly higher-quality anti-aliased images. In contrast to previous work, this article considers the more general case when the superimposition grid is nonuniform. It also presents key theoretical and practical results for general display supersampling.

Section 2 examines work related to the paradigm of display supersampling. Section 3 presents the framework used to model general DSS and points out the shortcomings of conventional anti-aliasing methods for supersampled displays. Section 4 analyzes DSS based on a novel filter bank perspective and derives the conditions for optimal rendering. We show that, to be able to reconstruct alias-free frequencies beyond the Nyquist frequency of any of the component images, the generated subframes must be aliased. Further, the subframes must be generated in such a way that the aliasing is engineered to cancel when the images are physically superimposed. We also formally prove that reconstruction of alias-free frequencies well beyond the fundamental Nyquist frequency of any single subframe is possible. We derive the optimal subframes that will perfectly cancel aliasing in the 1D case. In Section 5, we derive an iterative algorithm

---

Authors' addresses: N. Damera-Venkata and N. L. Chang, Hewlett-Packard Laboratories, 1501 Page Mill Road, MS 1203, Palo Alto, CA 94304; email: nelson.chang@hp.com.

Permission to make digital or hard copies of part or all of this work for personal or classroom use is granted without fee provided that copies are not made or distributed for profit or direct commercial advantage and that copies show this notice on the first page or initial screen of a display along with the full citation. Copyrights for components of this work owned by others than ACM must be honored. Abstracting with credit is permitted. To copy otherwise, to republish, to post on servers, to redistribute to lists, or to use any component of this work in other works requires prior specific permission and/or a fee. Permissions may be requested from Publications Dept., ACM, Inc., 2 Penn Plaza, Suite 701, New York, NY 10121-0701 USA, fax +1 (212) 869-0481, or permissions@acm.org. © 2009 ACM 0730-0301/2009/01-ART9 \$5.00 DOI 10.1145/1477926.1477935 <http://doi.acm.org/10.1145/1477926.1477935>

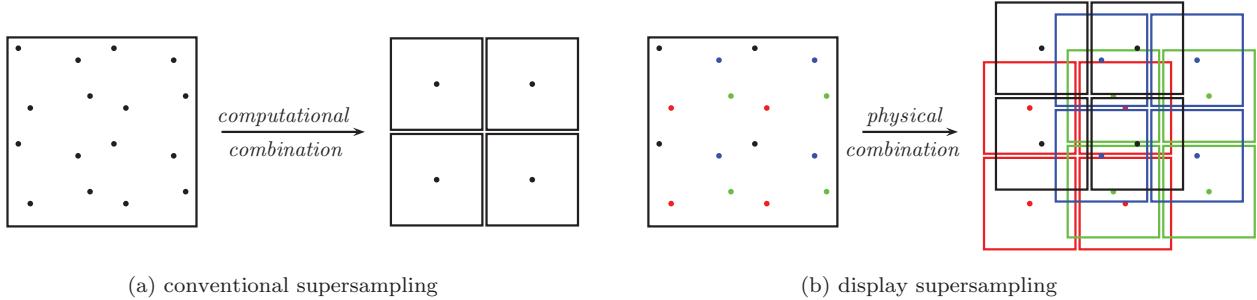


Fig. 1. Comparison of conventional and display supersampling. (a) In conventional supersampling, multiple scene samples are taken at different locations within a screen pixel and computationally combined via filtering to produce an anti-aliased image at the scene resolution. (b) In display supersampling, multiple subframes are generated and superimposed at subpixel shifted/warped offsets, where these offsets could be in general spatially varying. This creates *display* supersampling patterns similar to those used in conventional supersampling. Multiple display samples are combined by the physical summation of light to form the anti-aliased image.

for optimal subframe generation applicable to the 2D case and show that it indeed has the desired alias-cancellation property. It is capable of rendering high-resolution alias-free images on supersampled displays. We then present near-optimal, efficient, noniterative subframe generation algorithms based on the filter bank view of the optimal rendering task; these are suitable for real-time implementations. Section 6 considers a key embodiment of DSS: a scalable, high-brightness, high-resolution multiprojector superimposed display. In this case, we describe actual real-time implementations of the fast subframe generation methods on commodity graphics hardware. Finally, Section 7 concludes the article by summarizing the contributions and discussing their implications for high-quality anti-aliased rendering, texture mapping, and super-resolution.

## 2. RELATED WORK

The problem of rendering a high-resolution anti-aliased image on a display capable of superimposing multiple low-resolution images is closely related to classic problems in both computer graphics and computer vision. In computer graphics, polygons and textures need to be rendered without aliasing on displays with limited pixel resolution. Anti-aliasing and texture mapping methods strive to remove signal frequencies beyond the Nyquist frequency of the display to produce high-quality rendered images. In conventional supersampling [Crow 1981], multiple scene samples are taken at different locations within a screen pixel and computationally combined via filtering to produce an anti-aliased image at the scene resolution. By choosing jittered [Deering et al. 1988] or stochastic [Cook 1986; Dippe and Wold 1985] sampling locations, a high-quality anti-aliased image may be rendered. A frequency-domain analysis of supersampling is given in Mitchell [1987]. Commodity graphics hardware typically utilizes full-scene anti-aliasing (FSAA), where a high-resolution image of  $2\times$  to  $16\times$  the resolution of the desired screen image is rendered. This image is then filtered and reduced to the low-resolution screen image. With successive refinement [Fuchs et al. 1985], a multiscan-conversion approach is used, where the high-resolution image is not explicitly generated. The scene is first rendered at the display resolution. In subsequent passes, the images are again rendered at the display resolution. However, the samples are taken at subpixel offsets from the original samples. The samples at the end of each pass are merged to form the anti-aliased low-resolution image.

While these techniques seek to merge subpixel samples of a high-resolution scene computationally, DSS produces anti-aliased ren-

dering through subpixel merging via a physical summation of light intensity. The DSS patterns created by the superimposition of pixel centers are similar to the supersampling patterns used in conventional supersampling; Figures 1(a) and 1(b) compare conventional supersampling with DSS, respectively. Other conventional supersampling patterns such as RGSS and 8-Rooks can also be employed for display supersampling [Akenine-Möller and Haines 2002].

Texture mapping is used in computer graphics to map textures onto a surface. After the mapping is computed, the mapped image must be resampled to the uniform screen grid. In general, a square screen pixel has a curvilinear quadrilateral pre-image in texture space [Heckbert 1986]. The sampling density used to render a screen pixel is thus spatially nonuniform. In such a case, the anti-alias filtering must be performed using an anisotropic spatially varying filter that accounts for pixel profile deformation and sampling density variation [Heckbert 1989]. In multitexturing, multiple low-resolution textures may be combined to enhance texture mapping [Wang et al. 2001]. The DSS analog is the case of multiprojector superimposed projection, where the superimposed pixel centers form a nonuniform spatially varying display grid on which a high-resolution image (specified on a uniform grid) must be rendered.

Given a high-resolution image to be rendered, DSS seeks to compute the optimal low-resolution subframes, which, when superimposed, will produce an alias-free high-quality image that is as close as possible to the original high-resolution image. This problem may also be regarded as an inverse of the classic super-resolution problem in computer vision [Park et al. 2003], which infers a high-quality, high-resolution image from multiple blurred and sampled low-resolution camera views. The multiple views may be derived from subpixel shifted low-resolution image captures relative to a high-resolution scene using a jitter camera [Ben-Ezra et al. 2004], or may be related via higher-order geometric transformations in the case of arbitrary views [Elad and Feuer 1997; Irani and Peleg 1990; Zomet et al. 2001; Jiang et al. 2003].

While rigorous analyses of the theory and limits of camera super-resolution exist [Baker and Kanade 2002; Lin and Shum 2004], the analysis of display supersampling has been limited in scope. Previous work has shown the viability of super-resolution on supersampled displays only in the special case when the resulting superimposition grid is uniform [Majumder 2005; Said 2006]. We consider more general nonuniform sampling in this work.

There have been only a couple of examples in the literature of actual supersampled displays, both restricted to constant subframe shifts. Allen and Ulichney [2005] presented an approach in which

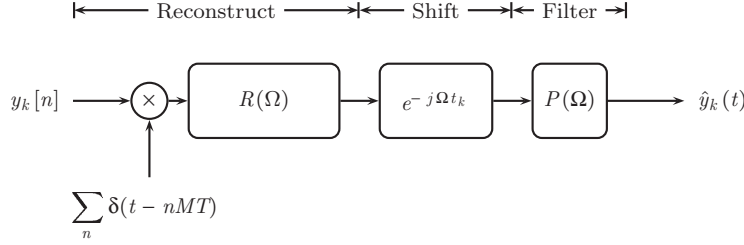


Fig. 2. 1D model of a single subframe. The discrete pixels are multiplied by a continuous impulse train with spacing  $MT$ , reconstructed with a reconstruction filter  $R(\Omega)$ , and bandlimited to the signal bandwidth  $W = \frac{\pi}{T}$ . Here,  $\hat{y}_k(t)$  may be sampled to obtain a discrete signal.

images from a light modulator are optically shifted (or wobbled) and projected in rapid succession so as to appear as if they are projected simultaneously and superimposed. They show that the perceived resolution may be increased with a wobbled low-resolution modulator without requiring a more expensive high-resolution one. Note that a close dual to the wobbled projectors is the previously mentioned jitter camera [Ben-Ezra et al. 2004].

Jaynes and Ramakrishnan [2003] considered the problem of multiprojector superimposed projection and demonstrated some resolution enhancement where the projectors overlapped. They approximate a warped subframe as the sum of regionally shifted subsampled images. Each such image is initially estimated in the frequency domain by phase shifting the frequencies of the target image to be rendered. Then, a greedy heuristic process is used to recursively update pixels with the most error globally. Jaynes and Ramakrishnan point out that this formulation not only is suboptimal, but also precludes real-time rendering applications because of its complexity. In contrast, we derive in this article an optimal provably convergent subframe generation algorithm that is shown to lead to efficient real-time rendering.

A key question when discussing multiprojector superimposition is how it compares with projector tiling [Raskar et al. 1999; Surati 1999; Majumder and Stevens 2005; Brown et al. 2005; Harville et al. 2006]. After all, much higher-resolution images can be rendered by simply tiling projectors. When display resolution and flexible aspect ratios are the important metrics, tiling is the best choice. As we will show in this article, there are fundamental limits to the resolution that can be achieved with superimposed projection, and superimposed projection cannot handle arbitrary aspect ratios. However, tiled projection compromises brightness and contrast in the overlap “blend” regions to achieve seamlessness. Also, if a single projector in a tiled system drifts or fails, the whole display is compromised. Thus, in cases when brightness, contrast, and robustness are paramount and the content resolution itself is limited, superimposition may be a preferred choice.

We recently showed that we can unify the theories of both tiled and superimposed projection, making it possible to support novel hybrid tiled and superimposed configurations [Damera-Venkata et al. 2007]. This allows us to utilize the best features of both paradigms.

### 3. MODELING DISPLAY SUPERSAMPLING

We derive the key theoretical results using a one-dimensional (1D) model presented in Section 3.1. The model is based on basic signal processing theory [Oppenheim and Schafer 1989]. It permits rigorous Fourier analysis, provides clear insights into the defining characteristics of supersampled displays, and forms the basis for developing practical 2D models and rendering algorithms. We present 2D models for DSS in Section 3.2. Simple rendering algorithms

based on point sampling and conventional anti-alias filtering, and their limitations, are described in Section 3.3.

#### 3.1 1D Model

For this analysis, we assume that the supersampled display consists of the superimposition of multiple subframes. In this case, modeling DSS reduces to the modeling of the image formation mechanism of a single image subframe. Assume that the reference class of signals to be rendered via DSS consists of continuous bandlimited signals  $\{x(t)\}$  with signal bandwidth  $W = \frac{\pi}{T}$ , where  $T$  represents the Nyquist sampling period. This class of continuous signals may be sampled at locations  $t = nT$  to obtain discrete signals  $x[n]$  without introducing aliasing. Figure 2 shows our modeling of an image subframe whose pixels are spaced  $MT$  apart ( $M$  times reference pixel spacing) and have a pixel point spread function represented by  $R(\Omega)$  in the frequency domain. Without loss of generality, the  $k$ th subframe is offset with respect to the zeroth subframe by a global shift  $t_k$ . The shift is represented in the frequency domain by a multiplication with the factor  $e^{-j\Omega t_k}$ . Here  $P(\Omega)$  represents a prefiltering operation on the subframe to obtain  $\hat{y}_k(t)$ .  $P(\Omega)$  is defined by

$$P(\Omega) = \begin{cases} 1 & |\Omega| \leq W \\ 0 & \text{else} \end{cases}. \quad (1)$$

We can think of this filter as representing the filtering performed by a hypothetical “eye.” By choosing it as a lowpass filter with bandwidth  $W$ , we imply that we do not care about spurious frequencies beyond the Nyquist frequency of the high-resolution signal (i.e., our hypothetical eye is tuned to the same resolution as the high-resolution signal). The signal  $\hat{y}_k(t)$  may be sampled uniformly at  $t = nT$  to convert it to a discrete-time signal  $\hat{y}_k[n]$  of the same size as  $x[n]$ .

With superimposition, the shifted component subframes are pre-filtered, and summed to obtain a simulation  $\hat{x}(t)$  of the rendered signal. For  $N$  subframes, we have

$$\hat{x}(t) = \sum_{k=0}^{N-1} \hat{y}_k(t). \quad (2)$$

This sequence of operations is reminiscent of texture resampling [Heckbert 1989]. In this case, however, the prefilter  $P(\Omega)$  does not bandlimit the signal to the Nyquist frequency of each subframe, but rather to the desired bandwidth of the high-frequency signal  $x(t)$ . Since  $y_k[n]$  is in general an undersampled version of  $x(t)$ ,  $\hat{y}_k(t)$  is in general a filtered and aliased version of  $x(t)$ . The 1D model described before sufficiently models display sampling, pixel profiles, and geometric distortion (viz. global shift in 1D).

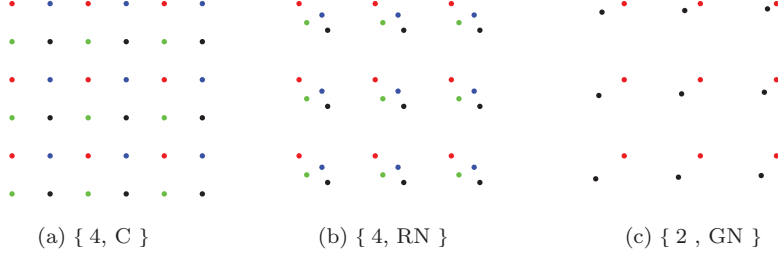


Fig. 3. Display supersampling configurations. The naming convention is {Number of superimposed subframes, Relative geometric distortion type (Critical sampling, Recurrent Nonuniform sampling, General Nonuniform sampling)}.

### 3.2 General 2D Models

Extending to 2D, shifts in the 1D model are replaced with generalized warps  $\mathbf{m}_k(\cdot)$ . Specifically,  $r(\cdot)$  and  $p(\cdot)$  represent the reconstruction filter and prefilter, respectively. The superimposed image may be modeled as a sum of resampled textures  $y_k[\mathbf{i}]$  as [Heckbert 1989]

$$\hat{x}[\mathbf{j}] = \sum_k \int_{\mathbf{t}} p(\mathbf{j} - \mathbf{t}) \sum_{\mathbf{i}} r(\mathbf{m}_k^{-1}(\mathbf{t}) - \mathbf{i}) y_k[\mathbf{i}] d\mathbf{t}, \quad (3)$$

where boldface represents 2D quantities. Eq. (3) may be simplified as

$$\hat{x}[\mathbf{j}] = \sum_k \sum_{\mathbf{i}} \rho_k(\mathbf{i}, \mathbf{j}) y_k[\mathbf{i}], \quad (4)$$

where the resampling filters  $\rho_k[\mathbf{i}, \mathbf{j}]$  are given by

$$\rho_k(\mathbf{i}, \mathbf{j}) = \int_{\mathbf{t}} p(\mathbf{j} - \mathbf{t}) r(\mathbf{m}_k^{-1}(\mathbf{t}) - \mathbf{i}) d\mathbf{t}, \quad (5)$$

$$= \int_{\mathbf{s}} p(\mathbf{j} - \mathbf{m}_k(\mathbf{s})) r(\mathbf{s} - \mathbf{i}) \left| \frac{\partial \mathbf{m}_k}{\partial \mathbf{s}} \right| d\mathbf{s}, \quad (6)$$

where the Jacobian  $\frac{\partial \mathbf{m}_k}{\partial \mathbf{s}}$  is introduced by a change of variables. The resampling filters may be computed based on Eq. (5) using numerical integration and stored, or may be computed efficiently on-the-fly using EWA filters [Heckbert 1989].

There are three essential parameters that define a DSS configuration: sampling, pixel profiles (i.e., pixel point spread functions), and geometric distortion. Typical displays employ rectangular sampling, and hence the focus shall be on this type of sampling.<sup>1</sup> A square PSF may be modeled by

$$r_{box}(\mathbf{u}) = \begin{cases} 1 & \left| \frac{u_x}{s} \right| \leq \frac{1}{2}, \left| \frac{u_y}{s} \right| \leq \frac{1}{2} \\ 0 & \text{else} \end{cases}, \quad (7)$$

where  $s$  represents the scale factor. Note that  $s \leq 1$  models the so-called “screen door” gap between adjacent pixels of DLP and LCD projectors. Finally, there are different DSS configurations that result from different relative geometric distortions between component image subframes.

- (1) *Critical Uniform Sampling*. This is shown in Figure 3(a), where the geometric distortion between component subframes is defined by global shifts and when the shifts result in a uniform pixel grid (with no overlapping pixel centers) identical to the pixel grid of the high-resolution image to be rendered.

<sup>1</sup>It is worth noting that our analysis also applies to more general display sampling geometry such as Quincunx sampling.



Fig. 4. Section of original 1920x1080 image from the “Animusic” sequence used in experiments. ©2007 Animusic. Images used with permission ([www.animusic.com](http://www.animusic.com)).

- (2) *Recurrent Nonuniform Sampling*. We show this in Figure 3(b), where the geometric distortion between component subframes is again defined by global shifts, but these shifts do not result in a uniform sampling grid after superimposition. This case arises with jittered displays.
- (3) *General Nonuniform Sampling*. This is seen in Figure 3(c), where the geometric distortion between component subframes is space varying and the sampling grid resulting from superimposition is nonuniform. This case arises with multiprojector superimposition.

It should be clear that each described configuration is a superset of the configurations above it. The remainder of the article shall analyze the first two configurations and provide experimental results for the third configuration.

### 3.3 Naïve Subframe Generation

With the DSS framework in place, the challenge is then the so-called *subframe generation problem*: Generate the appropriate low-resolution subframes  $y_k[n]$ , given a high-resolution input image  $x[n]$ . We motivate the need for better understanding and optimal algorithms by way of examples derived via naïve subframe generation techniques. Figure 4 shows a 100 × 100 pixel section of an example image on a rectangular display grid and is the target high-resolution image to be rendered for the remainder of the article. Figures 5(a) and 5(b) show low-resolution subframe images directly derived from this image via nearest-neighbor sampling and

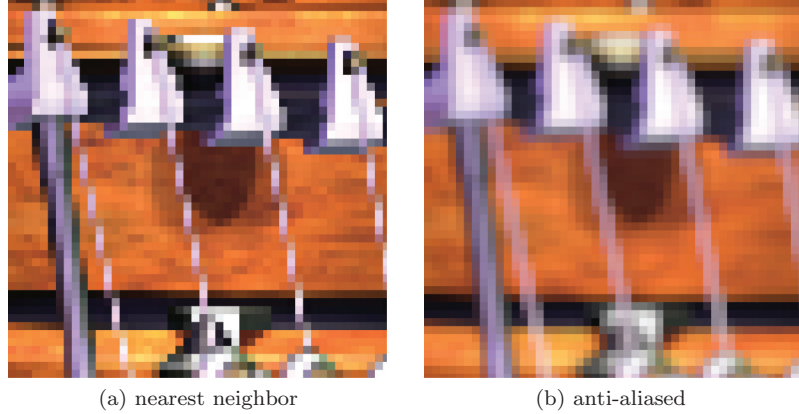


Fig. 5. Low-resolution subframes generated from Figure 4 using naïve subframe generation via: (a) nearest-neighbor sampling; and (b) Gaussian anti-alias filtering.

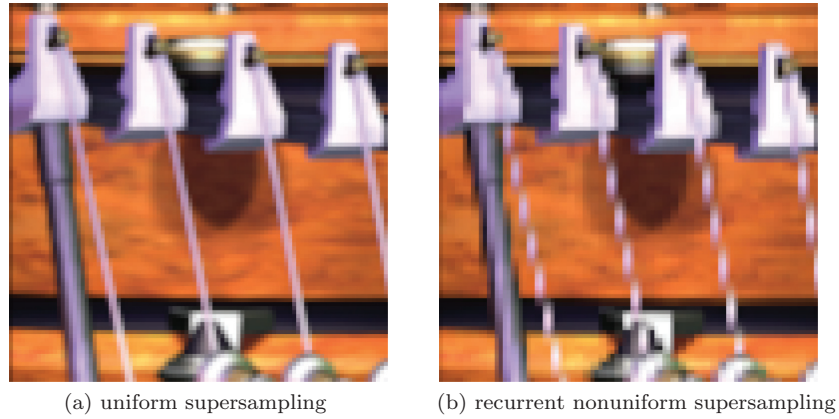


Fig. 6. Result of nearest-neighbor sampling in the case of uniform and recurrent nonuniform display supersampling. Note that (a) is alias-free while (b) appears aliased.

Gaussian anti-alias filtering followed by sampling, respectively.<sup>2</sup> The nearest-neighbor sampled, low-resolution image exhibits clear aliasing artifacts (indicated by the jagged edges), whereas the anti-aliased image does not have the jagged edges but appears more blurred due to loss of high-frequency information.

Once computed, the subframes are superimposed together to form the DSS approximation of the target image. We consider the resulting images obtained via naïve subframe generation techniques. First, a nearest-neighbor approach directly samples the high-resolution image to create low-resolution subframes. Figures 6(a) and 6(b) show superimposed modeling results for four low-resolution subframes with the relative display supersampling geometry of Figure 3(a) and 3(b), respectively. We see that this approach produces aliased results for recurrent nonuniform sampling, but alias-free results in the case of critically sampled geometries. Even though individual subframes are aliased (recall Figure 5(a)), it is easy to see why the critically sampled case still produces alias-free results: Using nearest-neighbor sampling, every sample is picked up

from an integer high-resolution location, meaning that the rendered image is simply a filtered version of the given high-resolution image.

We could instead anti-alias each subframe (recall Figure 5(b)) and then superimpose these subframes to form the final image. Figure 7(a) and 7(b) show the corresponding results using a conventional anti-aliasing approach to filter and sample the high-resolution image to create low-resolution subframes. In both cases, the superimposed rendered result is alias-free but appears blurry. Moreover, this technique produces worse results than nearest-neighbor sampling for critically sampled geometries.

The simple experiments described raise key questions: Can high-quality alias-free images be produced on supersampled displays with arbitrary sampling, and if so, by what mechanism? Can we reconstruct frequencies beyond the Nyquist frequency of a component subframe? The subsequent section develops theory to answer these fundamental questions.

#### 4. THEORETICAL ANALYSIS

In this section, we analyze DSS using the 1D signal processing model presented in Section 3.1. We analyze naïve subframe generation algorithms in more detail and explain why they fail to produce high-quality images on supersampled displays. Criteria for optimal,

<sup>2</sup>All subframes in this work are reconstructed with a box kernel and resampled for display at the same resolution as the original high-resolution image to facilitate comparison.

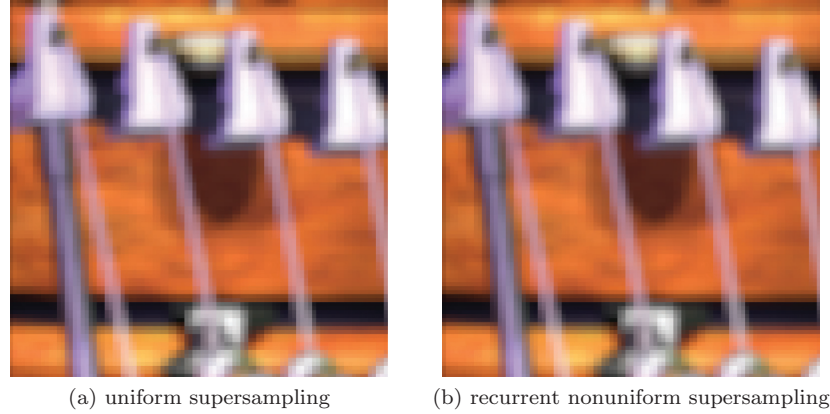


Fig. 7. Result of anti-aliasing the subframes in the case of uniform and nonuniform display supersampling. Note that both (a) and (b) are alias-free but blurred.

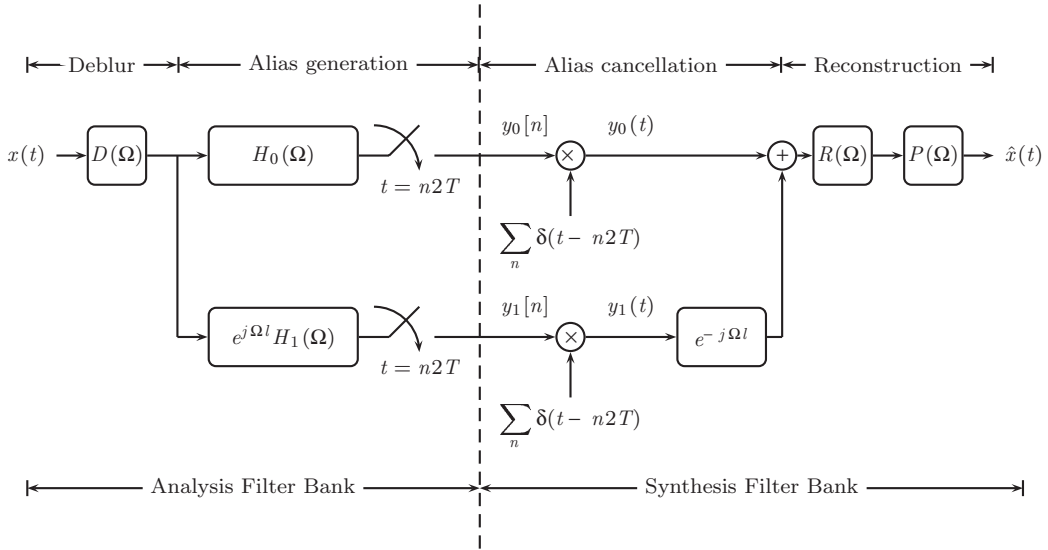


Fig. 8. 1D model for the superimposition of two subframes. The synthesis bank follows directly from summing two instantiations of the 1D single projector model discussed in Section 3.1. The analysis bank is introduced to generate low-resolution subframes from a high-resolution signal  $x(t)$ . The deblurring filter  $D(\Omega)$  precompensates for the blur introduced by the pixel PSF  $R(\Omega)$ , while the alias-generation filters  $H_k(\Omega)$  are designed to cancel the aliasing of the synthesis bank. The operation immediately following the filtering step with  $H_k(\Omega)$  is the sampling step. Subframes are sampled at twice the sampling period ( $2T$ ) of the high-resolution signal. This relative undersampling generates aliasing.

high-resolution, anti-aliased rendering are derived. We show that optimal anti-aliased rendering may be accomplished by designing an analysis filter bank with alias-cancellation and deblurring properties. A closed-form solution is presented and analyzed for the optimal alias-canceling subframes in the recurrent nonuniform sampling case.

For convenience and clarity, we first consider a supersampled display comprising just two component image subframes, before considering the more general  $N$  subframe case. Given subframes  $y_k[n]$ , we can use the 1D model of Section 3.1 to simulate the superimposed output signal via summation. This model may be represented by the synthesis filter bank shown in the right half of Figure 8. Without loss of generality, we have assumed that one of the subframes is the reference subframe with global shift  $t_0 = 0$ . The second subframe is assumed shifted with respect to the input signal by  $t_1 = l < 2T$ . Further, since the filters  $R(\Omega)$  and  $P(\Omega)$  are shift-invariant, they

may be allowed to operate after the shift (compare Figures 2 and 8) without changing the output. This is convenient, since it allows the effects of the reconstruction filter (and prefilter) to be decoupled from nonuniform sampling effects. While such decoupling is technically only valid for the case of recurrent nonuniform sampling (where we assume spatially invariant global shifts between projectors), it allows for rigorous closed-form theoretical analysis and provides key intuition about the nature of the general problem with spatially varying shifts. Section 5 presents algorithms that simultaneously account for both aliasing and blurring introduced in the general spatially varying nonuniform sampling case.

The continuous spectrum of the output signal in Figure 8 is given by

$$\hat{X}(\Omega) = P(\Omega) R(\Omega) (Y_0(\Omega) + e^{-j\Omega l} Y_1(\Omega)). \quad (8)$$

In this case,  $\hat{X}(\Omega)$  is the sum of the shifted spectra of the two subframes multiplied by the spectrum of the reconstruction filter and bandlimiting prefilter. The subframe generation problem then reduces to choosing  $Y_0(\Omega)$  and  $Y_1(\Omega)$  so that  $\hat{X}(\Omega)$  is as close as possible to  $X(\Omega)$ . Since the physical signal reconstruction is represented as a synthesis bank, we introduce a corresponding analysis bank (shown on the left half of Figure 8) for the signal generation process, where the filters  $D(\Omega)$ ,  $H_0(\Omega)$ , and  $H_1(\Omega)$  are design parameters. Figure 8 shows the proposed model for signal generation and reconstruction viewed as a complete filter bank with both analysis and synthesis components.

Since we decoupled the effect of the reconstruction filter from the effect of nonuniform sampling in the synthesis filter bank, we have similarly decoupled the deblurring filter  $D(\Omega)$  from the alias-generation filters  $H_k(\Omega)$  in the analysis filter bank.  $D(\Omega)$  compensates for the blurring introduced by the reconstruction filter  $R(\Omega)$ . The alias-generation filters  $H_k(\Omega)$  compensate for the aliasing introduced by the nonuniform sampling modeled by the synthesis filter bank.

With this filter bank model in mind, we can analyze different subframe generation techniques more fully and better understand the reasons for the results in Figures 6 and 7. Section 4.1 presents an analysis of point sampling based on the filter bank model described previously and explains why it performs well for uniform critically sampled geometries but produces aliased results with nonuniform geometries. Section 4.2 shows why conventional anti-aliasing methods fail in rendering high-quality anti-aliased images on supersampled displays. Section 4.3 derives optimal subframe generation as an optimal deblurring and alias-cancellation procedure. Section 4.4 discusses the interaction between the blurring introduced by the reconstruction filter and the aliasing due to the (recurrent) nonuniform sampling geometry. This last section presents the mechanism by which alias-free signals beyond the Nyquist frequency of any individual subframe may be produced and explores fundamental limits to such super-resolution.

#### 4.1 Analysis of Nearest-Neighbor Point Sampling

For nearest-neighbor point sampling,  $D(\Omega) = H_0(\Omega) = H_1(\Omega) = 1$  in Figure 8. Since each subframe is an undersampled version of the original signal  $X(\Omega)$ , each subframe is aliased. Eq. (8) reduces to

$$\hat{X}(\Omega) = C P(\Omega) R(\Omega) \sum_{n=-\infty}^{\infty} X(\Omega - nW) e^{-jWnl} \cos\left(\frac{Wnl}{2}\right), \quad (9)$$

where  $C$  is a constant term, and  $W = \frac{\pi}{T}$  is the Nyquist frequency of  $X(\Omega)$ . In the case of critical sampling,  $l = T$  and Eq. (9) becomes

$$\hat{X}(\Omega) \propto P(\Omega) R(\Omega) \sum_{n=-\infty}^{\infty} X\left(\Omega - \frac{\pi n}{T}\right) e^{-j\pi n} \cos\left(\frac{\pi n}{2}\right). \quad (10)$$

The terms that correspond to odd values of  $n$  vanish in the superimposition due to the cosine factor. This means that although each subframe  $Y_k(\Omega)$  is aliased, the aliasing is actually canceled in the superimposed rendering; this is illustrated in Figure 9, where the dotted lines indicate the terms that vanish. To the contrary, in the case of nearest-neighbor signal generation for noncritically sampled geometries (e.g.,  $l = \frac{T}{2}$ ), the odd terms do not vanish, and the rendered image appears aliased. Moreover, they appear blurred due to the effect of the reconstruction filter. These findings are consistent with the results shown in Figure 6.

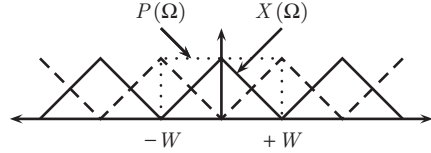


Fig. 9. Example image spectra for the nearest-neighbor case. The high-resolution signal spectrum is shifted and replicated at integer multiples of  $W$  (see Eq. (9)). This leads to aliased output in general. However, alias cancellation occurs in the case of nearest-neighbor critical sampling with  $l = T$  (see Eq. (10)). High-resolution image spectra centered at even multiples of  $W$  are shown with solid lines. Image spectra centered at odd multiples of  $W$  vanish (see dashed lines) in the rendered image. Thus, the prefilter reconstructs the alias-free baseband spectrum to recover the high-resolution image blurred with the reconstruction filter  $R(\Omega)$  (not shown in the figure).

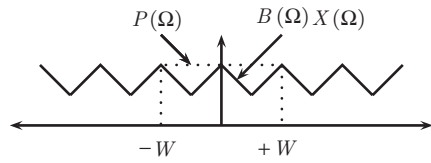


Fig. 10. Example image spectra to analyze the anti-alias/texturing filtering case. Applying conventional anti-alias/texturing filtering to generate the subframes successfully eliminates aliasing, but chops off high-resolution signal frequencies (see Eq. (12)) since the anti-alias filter  $B(\Omega)$  has bandwidth  $\frac{W}{2}$  (see Eq. (11)). Image spectra centered at odd multiples of  $W$  do not vanish or interfere with the spectra centered at the even multiples. However, effective bandwidth of the rendered signal is no more than that of a single projector, in spite of the extra display samples. Note that some reconstruction artifacts will exist since the reconstruction filter  $R(\Omega) \neq B(\Omega)$  in general.

#### 4.2 Analysis of Conventional Anti-Aliasing Methods

We now examine conventional anti-aliasing methods. In this case,  $D(\Omega) = 1$ ,  $H_0(\Omega) = H_1(\Omega) = B(\Omega)$ , where  $B(\Omega)$  is an ideal anti-alias lowpass filter defined by

$$B(\Omega) = \begin{cases} 1 & |\Omega| \leq \frac{W}{2} \\ 0 & \text{else} \end{cases}. \quad (11)$$

The spectrum of the rendered image is then given by

$$\begin{aligned} \hat{X}(\Omega) &\propto P(\Omega) R(\Omega) \sum_{n=-\infty}^{\infty} B(\Omega - nW) \\ &\times X(\Omega - nW) e^{-jWnl} \cos\left(\frac{Wnl}{2}\right). \end{aligned} \quad (12)$$

The anti-alias filter guarantees that the individual subframes will not be aliased for any  $l$ . However, we see from Eq. (8) that  $\hat{X}(\Omega)$  cannot reproduce any higher frequencies than those reproducible by an individual component subframe. This implies that although the rendered image is alias-free, it is limited by the Nyquist frequency of a single subframe. The anti-alias filter chops off signal frequencies higher than  $\frac{W}{2}$  so that the rendered image does not benefit from the increased sampling density afforded by DSS; Figure 10 illustrates this case (recall the corresponding results shown in Figure 7).

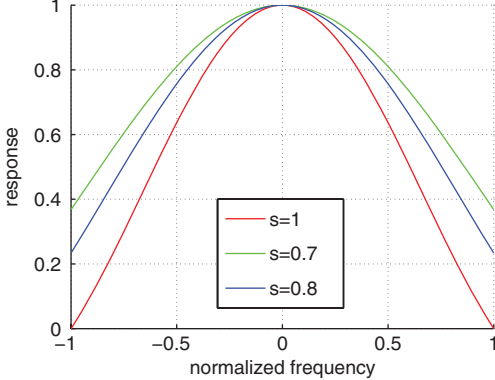


Fig. 11. Frequency profile of the reconstruction filter. The filter is modeled as a rectangular box kernel with parameter  $s$  that controls its duty cycle (e.g.  $s = 1$  corresponds to full coverage with no “screen door” gap;  $s = 0.8$  corresponds to a pixel with 80% duty cycle and a 20% screen door gap). The frequency scale is normalized by the signal bandwidth  $W$ .

### 4.3 Analysis of Optimal Subframe Generation

Referring back to the filter bank model in Figure 8, Eq. (8) for the general case reduces to

$$\hat{X}(\Omega) \propto P(\Omega)R(\Omega) \sum_{n=-\infty}^{\infty} D(\Omega - nW)X(\Omega - nW)(H_0(\Omega - nW) + H_1(\Omega - nW)e^{j(\Omega - nW)t}e^{-j\Omega t}). \quad (13)$$

The goal then is to find reconstruction filter  $D(\Omega)$  and subframe generation filters  $H_k(\Omega)$ . We consider these tasks independently.

**4.3.1 Compensating for the Reconstruction Filter.** The role of  $D(\Omega)$  is to compensate for the frequency attenuation effects of the reconstruction filter  $R(\Omega)$ . Assuming a rectangular box reconstruction filter profile given by the 1D equivalent of Eq. (7), we can plot its frequency response for different values of  $s$  (see Figure 11), where  $s$  models the screen-door effect by controlling the duty cycle. A smaller  $s$  corresponding to a larger screen-door gap between pixels results in a larger bandwidth for the reconstruction filter and less frequency attenuation. The worst case is when  $s = 1$  (i.e., there is no screen-door gap). Since the subframes  $y_k(t)$  in Figure 8 have sampling periods twice that of the Nyquist period of the original signal  $x(t)$ , the Nyquist frequency of the subframes is at  $\Omega = \frac{W}{2}$  relative to the original signal’s Nyquist frequency of  $\Omega = W$ . Thus, we see from Figure 11 that even in the worst-case frequency attenuation scenario when pixel fill is 100%, the reconstruction filter does not completely cut-off super-Nyquist subframe frequencies  $\Omega > \frac{W}{2}$ .

A simple conceptual model for  $D(\Omega)$  is the inverse frequency profile of the reconstruction filter profile shown in Figure 11. If we further place the restriction that the output resulting from filtering with  $D(\Omega)$  is in the range  $[0, 1]$ , then the profiles of Figure 11 directly represent the maximum amplitudes of sinusoids at various frequencies that can be precompensated to perfectly eliminate frequency attenuation due to the reconstruction filter. Thus, a range of signal frequencies that are beyond the Nyquist frequency of the subframes (i.e., sinusoids of frequencies outside  $[-0.5, 0.5]$  with amplitudes equal to  $R(\Omega)$ ) may be perfectly compensated for the effects of the reconstruction filter (i.e.,  $R(\Omega)D(\Omega)X(\Omega) \approx X(\Omega)$ ). The area of the PSF curve outside the range  $[-0.5, 0.5]$  shows that this super-Nyquist resolution is significant. In general, regularized inverse filters constitute a more intelligent choice than simply clip-

ping the outputs of ideal inverse filters, since they avoid wasting signal energy on frequencies/amplitudes that cannot be reproduced anyway (see Said [2006] for a detailed discussion of the properties of regularized 1D inverse reconstruction filters).

In practice, unlike high-frequency alternating grill patterns that have full-scale signal amplitude excursions, most natural images do not exhibit full-amplitude high-frequency signal excursions. Thus, precompensating for the reconstruction filter via deblurring recovers significant high-frequency information on most natural images. This claim is illustrated by example in Section 5.

**4.3.2 Optimal Alias Cancellation.** Given a high-resolution signal that has been precompensated for the effects of the reconstruction filter as discussed in Section 4.3.1, we must split it into low-resolution subframes  $y_k(t)$ . We do so using subframe generation filters  $H_k(\Omega)$  to cancel the aliasing introduced due to nonuniform display sampling. We may derive a closed-form representation of the optimal subframe generation filters  $H_k(\Omega)$ ,  $k = 0, 1, \dots, N - 1$  in the case of recurrent nonuniform sampling.

**THEOREM 4.1.** *A finite energy signal  $x(t)$ , bandlimited such that  $X(\Omega) = 0$ ,  $|\Omega| > W = \frac{\pi}{T}$ , may be split into  $N$  subframes,  $y_k(t)$ , which when superimposed at relative shift offsets  $t_k$ ,  $k = 0, 1, \dots, N - 1$ , exactly reproduce the original signal if the average display sampling period of the superimposed system is less than or equal to the Nyquist period  $T$  of the signal  $x(t)$ . The optimal subframes  $y_k(t)$  may be generated using the following equations.*

$$w_k(t) = (x \star h_k)(t) \quad (14)$$

$$y_k(t) = \sum_{n=-\infty}^{\infty} w_k(nNT)\delta(t - nNT) \quad (15)$$

$$h_k(t) = a_k \frac{\prod_{q=0}^{N-1} \sin(\pi(t + t_q - t_k)/NT)}{\pi t/NT} \quad (16)$$

$$a_k = \frac{1}{\prod_{q=0, q \neq k}^{N-1} \sin(\pi(t_q - t_k)/NT)} \quad (17)$$

The proof of this theorem is given in the Appendix. This result may be seen as the dual of the generalized sampling theorem for reconstructing a signal from nonuniform samples.

We illustrate the alias-cancellation properties of the aforesaid filters for the two ( $N = 2$ ) subframe case. The optimal subframe generation filter coefficients are

$$h_0(t) = \frac{\sin(\frac{\pi t}{2T}) \sin(\frac{\pi(t+l)}{2T})}{(\frac{\pi t}{2T}) \sin(\frac{\pi l}{2T})}. \quad (18)$$

$$h_1(t) = -\frac{\sin(\frac{\pi t}{2T}) \sin(\frac{\pi(t-l)}{2T})}{(\frac{\pi t}{2T}) \sin(\frac{\pi l}{2T})}. \quad (19)$$

In the frequency domain, these filters become

$$H_0(\Omega) = C \left\{ \frac{e^{j\pi l}}{2j} B\left(\Omega - \frac{W}{2}\right) - \frac{e^{-j\pi l}}{2j} B\left(\Omega + \frac{W}{2}\right) \right\}, \quad (20)$$

$$H_1(\Omega) = C \left\{ \frac{e^{j\pi l}}{2j} B\left(\Omega + \frac{W}{2}\right) - \frac{e^{-j\pi l}}{2j} B\left(\Omega - \frac{W}{2}\right) \right\}, \quad (21)$$

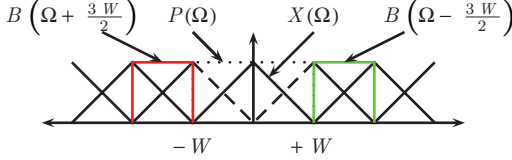


Fig. 12. Example image spectra to illustrate optimal alias-cancellation for  $0 < l < 2T$  (see Eq. (23)). The high-resolution image spectrum is replicated at integer multiples of  $W$ . However, the baseband high-resolution image spectrum survives without aliasing since when  $n = \pm 1$ , the contribution of the replicas centered at  $\Omega = \pm W$  to the baseband spectrum vanish (see dashed lines). This is because they do not fall in the passband of the surviving terms  $B(\Omega \mp \frac{3W}{2})$  (shown in green and red, respectively). The prefilter reconstructs the baseband spectrum to recover  $D(\Omega)R(\Omega)X(\Omega) \approx X(\Omega)$ , where  $D(\Omega)$  is the best approximation inverse filter to  $R(\Omega)$ .

where  $B(\Omega)$  is defined in Eq. (11). Notice that the optimal analysis filters have piecewise constant frequency responses in the range  $[-\frac{W}{2}, \frac{W}{2}]$  and are bandlimited to  $[-W, W]$ . This means that each channel of the filter bank will be aliased. We may now substitute Eqs. (20) and (21) into Eq. (13) to obtain the spectrum of the superimposed image.

$$\hat{X}(\Omega) \propto P(\Omega)R(\Omega) \sum_{n=-\infty}^{\infty} D(\Omega - nW)X(\Omega - nW) e^{-\frac{-j\pi nl}{2T}} \\ \left\{ \sin\left(\frac{\pi l(1+n)}{2T}\right) B\left(\Omega - nW - \frac{W}{2}\right) \right. \\ \left. + \sin\left(\frac{\pi l(1-n)}{2T}\right) B\left(\Omega - nW + \frac{W}{2}\right) \right\} \quad (22)$$

For signals that have been perfectly precompensated for the reconstruction filter  $R(\Omega)D(\Omega)X(\Omega) = X(\Omega)$ , we have

$$\hat{X}(\Omega) \propto P(\Omega) \sum_{n=-\infty}^{\infty} X(\Omega - nW) e^{-\frac{-j\pi nl}{2T}} \\ \left\{ \sin\left(\frac{\pi l(1+n)}{2T}\right) B\left(\Omega - nW - \frac{W}{2}\right) \right. \\ \left. + \sin\left(\frac{\pi l(1-n)}{2T}\right) B\left(\Omega - nW + \frac{W}{2}\right) \right\}. \quad (23)$$

With the optimal choice of subframes, the replica of the high-resolution image spectrum at  $n = 0$  survives, since the piecewise contributions of replicas at  $n = -1$  and  $n = 1$  to the baseband vanish for arbitrary shifts  $l$ . Figure 12 illustrates the alias-cancelling behavior of the optimal filters for an arbitrary  $0 < l < 2T$ . This case is also interesting because the special case of  $l = \frac{T}{2}$  was analyzed in Majumder [2005], where it was concluded that aliasing could not be eliminated. We show that if we consider the possibility of optimal subframe generation, aliasing can in fact be cancelled, allowing reconstruction of frequencies beyond the Nyquist frequency of a single subframe. We demonstrate the alias cancellation by the following example.

*Example 4.1.* Let  $N = 2$ ,  $T = 1$ , and  $l = 0.5$ . Let  $x(t) = A((\cos(2\pi ft) + 1)/2) + (0.5 - A/2)$  with  $A = 0.5$  and normalized frequency  $f = 0.8$  (the Nyquist frequency of the input sinusoid is normalized to 1). Note that the input signal frequency is beyond the Nyquist frequency of any of the subframes (viz. 0.5).

This example demonstrates that aliasing effects of the nonuniform sampling may indeed be cancelled by a proper choice of subframes

to produce alias-free super-Nyquist frequencies. Subframes were generated using discrete versions of the ideal filters of Theorem 4.1. Figure 13(a) shows the two aliased subframes  $y_k(t)$ , and Figure 13(b) shows the reconstructed  $\hat{x}(t)$ .<sup>3</sup> Despite  $y_k(t)$  being aliased,  $x(t)$  and  $\hat{x}(t)$  are found to be virtually identical. The alias cancellation can also be clearly seen in the frequency domain, where the subframes in Figure 13(c) have an alias component at  $f = 0.2$  that is eliminated in the superimposed result of Figure 13(d).

In this section, we have showed that in the case of recurrent nonuniform sampling, we can generate subframes that are themselves severely aliased, but combine to form alias-free high-resolution images through DSS. If the low-resolution pixel reconstruction filter bandwidth is greater than the Nyquist frequency of the low-resolution image, each low-resolution image can be engineered to contribute frequencies higher than its Nyquist frequency. Of course, this means that each subframe will have low-frequency aliasing. By properly generating the complementary subframes, we can cancel the low-frequency aliasing and reconstruct alias-free high frequencies that are beyond the Nyquist frequency of a single subframe. The subframe generation process can be thought of as similar to the alias-cancellation that occurs in filter bank theory [Strang and Nguyen 1996].

#### 4.4 Analysis of Resolution Gain

This section briefly discusses resolution limits of display supersampling; more details on the effects of physical image signal range limits on resolution gain in the 1D case are presented in Damera-Venkata and Chang [2007a]. Figure 14(a) and 14(b) illustrate the key factors affecting the frequency response of the rendered image in the 1D case when each component subframe is half the resolution of the high-resolution image to be rendered and pixel reconstructions are performed with a box function. The frequency scale has been normalized by the high-resolution bandwidth  $W$ .

Figure 14(a) illustrates the link between display sampling and aliasing. The red drawing shows the frequency response of a typical box reconstruction filter with  $s = 1$ . We see that it has a larger bandwidth (it first goes to zero at  $\Omega = W$ ) than the Nyquist frequency  $\frac{W}{2}$  of individual subframes. This means that subframe frequencies beyond  $\frac{W}{2}$  will be aliased (see dashed blue lines). Also from Figure 11, it is shown that a large pixel size results in heavy frequency attenuation while a small pixel size allows more image frequencies to pass. Figure 14(b) shows the effect of pixel size. It is easy to appreciate that, even if the Nyquist frequency of the display is high, allowing alias-free high frequencies, a large pixel size will simply kill these frequencies in the superimposed result. As we increase the number of subframes in DSS, the effective Nyquist frequency of the display increases. However, its frequency response is a limiting factor, since the effect of the reconstruction filter is multiplicative in the frequency domain (see Eq. (8)). If the reconstruction filter has zeros, these frequencies can never be recovered via DSS, even if more subframes are added.

With no DSS, sampling density is the major limiting factor, since the pixel size often has a greater bandwidth than the Nyquist frequency of the display (as shown in Figure 14). In this case, high-resolution images must be bandlimited to the Nyquist frequency to

<sup>3</sup>All discrete signals have been reconstructed with ideal sinc interpolation at an 8× oversample factor relative to  $x[n]$ . This step eliminates postaliasing artifacts introduced by MATLAB's default connect-the-dots reconstruction. Also, the infinite impulse responses of Theorem 4.1 were truncated using appropriate Hamming windows for the implementation.

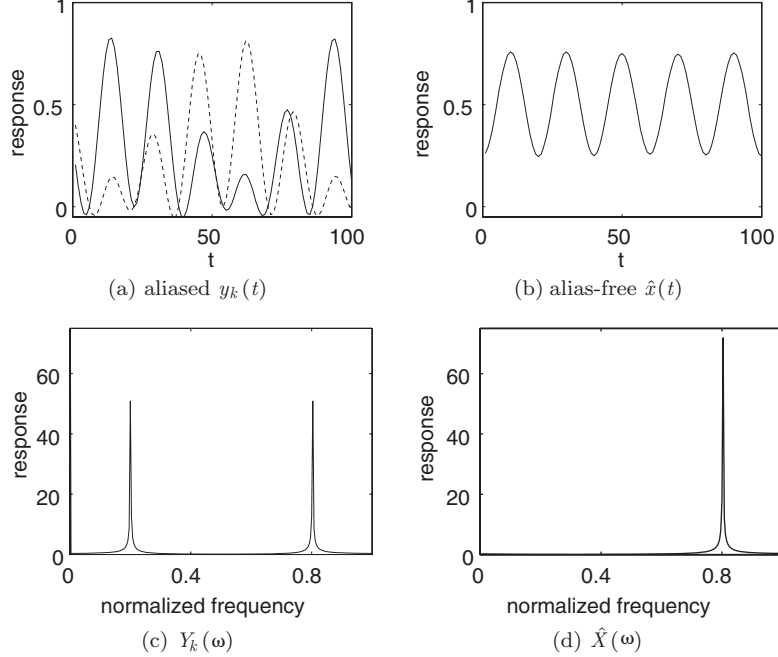


Fig. 13. Super-Nyquist results of Example 4.1. The frequency spectra are normalized by the Nyquist frequency of the high-resolution signal. The Nyquist frequency of a subframe occurs at  $f = 0.5$ . Frequencies beyond  $f = 0.5$  are regarded as super-Nyquist subframe frequencies. Subframes generated to reproduce super-Nyquist subframe frequencies are aliased (a), but combine to reproduce an alias-free super-Nyquist result (b). In the frequency domain, a low-frequency alias is present in the subframes (c) but is eliminated when the two subframes are combined via superimposition (d).

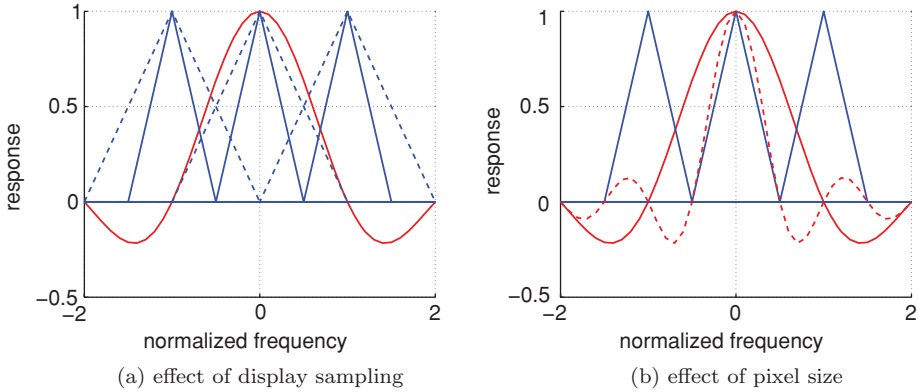


Fig. 14. Effects of sampling frequency and pixel size: (a) When sampling frequency is decreased below the Nyquist limit, aliasing occurs (dashed blue lines). The Nyquist frequency of a subframe is 0.5. Note that the frequency response of a square pixel (shown in red) allows frequencies higher than the Nyquist frequency. However, these subframe frequencies will be aliased. (b) When the pixel size is increased, the pixel profile in the frequency domain becomes narrower (dashed red line), causing frequency attenuation. Both aliasing and pixel size therefore impose constraints on the final image resolution.

prevent aliasing. In contrast, with DSS, we can have greater sampling density but introduce limits due to pixel size.

In practice, resolution limits arise from both the inability to perfectly compensate for the reconstruction filter (as discussed in Section 4.3.1) and the inability to perfectly cancel aliasing without exceeding the  $[0, 1]$  subframe signal range. The latter case was analyzed in Damera-Venkata and Chang [2007a], where we showed that, even if we were able to perfectly compensate for the effects of the reconstruction filter, resolution is often limited by the finite sub-

frame signal range. The reason is that subframe signals that exceed the subframe signal range must be clipped, leading to distortion. We also showed that such aliasing limits can be significantly relaxed by introducing more subframes, effectively increasing the oversampling rate. Thus, the PSF analysis of Section 4.3.1 forms a natural upper-bound analysis of the resolution that can be achieved by any configuration. Note that alias-cancellation ability depends on the relative geometry of the subframes. As we showed in Section 4.1 in the case of critical uniform sampling, perfect alias-cancellation is

possible, so resolution is only limited by the reconstruction filter profile. In the practical nonuniform sampling case, it may be impossible for a particular configuration of subframes to perfectly cancel aliasing for *all* signal amplitudes and frequencies without exceeding the  $[0, 1]$  subframe signal range. In this case, aliasing (apart from the PSF) also limits the class of super-Nyquist signal amplitudes and frequencies for which perfect reconstruction is possible.

Using a smaller pixel size with smaller duty cycle allows for more signal frequencies and amplitudes to be perfectly compensated for the effects of the reconstruction filter, whereas adding subframes allows for better alias-cancellation. While there are limits to the perfectly reproducible resolution, super-Nyquist frequencies and amplitudes may still be accurately recovered (even in the worst case of 100% duty cycle pixels), and thus significant super-Nyquist resolution gain is theoretically feasible.

We analyzed in this section recurrent nonuniform sampling in 1D, allowing us to decouple the effects of the reconstruction filter and the sampling geometry, for theoretical analysis. In the case of general nonuniform sampling, such decoupling is not possible. Further, the formulation of Theorem 4.1 does not explicitly factor in any physical constraints on the subframe values (e.g., negative input values for a projector are meaningless and unachievable), making it unsuitable as a practical subframe generation algorithm. The purpose of the preceding theoretical analysis was to provide insights into the mechanism by which super-resolution is achieved, namely deblurring and alias cancellation, and to discuss their impact on resolution limits. Majumder [2005] uses a similar 1D critical nonuniform sampling model to theoretically model and draw conclusions about general multiprojector super-resolution. Jaynes and Ramakrishnan [2003] model general projector super-resolution by recurrent nonuniform sampling over image regions/blocks. This allows subframe generation based on the FFT. In general, the superimposed image is subject to spatially varying blur and aliasing, precluding closed-form solutions. Iterative methods and fast spatially varying single-pass algorithms are discussed in the next section that attempt to simultaneously deblur and cancel aliasing in this general case. These algorithms provide concrete validation that significant resolution gain is practically achievable with DSS.

## 5. SUBFRAME GENERATION ALGORITHMS

In this section, we derive practical subframe generation algorithms that can be applied to arbitrary DSS configurations in 2D (i.e., arbitrary projector warps  $\mathbf{m}_k(\cdot)$  lead to general nonuniform sampling). We assume full duty cycle pixels (the worst case for resolution enhancement) and still show that significant super-Nyquist resolution gains are achievable. Section 5.1 presents an iterative algorithm for optimal subframe generation. Section 5.2 derives a near-optimal, efficient, noniterative algorithm for subframe generation that enables real-time performance. Subframe generation is achieved by a bank of filters designed to have compact support and incorporates both alias-cancellation and deblurring.

### 5.1 Iterative Subframe Generation

Given a desired target high-resolution image  $x[\mathbf{j}]$  to be rendered by the superimposed system, the rendering task is to determine the optimal subframes so that the final image formed on the supersampled display is as close as possible to the given image. Recall, superimposition of  $N$  component subframes may be modeled by Eq. (4). The optimal estimates for the subframes,  $\{\mathbf{y}_k^*\}$ , may be obtained as

solutions to the following optimization problem.

$$\{\mathbf{y}_k^*[\mathbf{i}]\} = \operatorname{argmin}_{\{\mathbf{y}_k[\mathbf{i}]\}} J = \operatorname{argmin}_{\{\mathbf{y}_k[\mathbf{i}]\}} \sum_{\mathbf{j}} (x[\mathbf{j}] - \hat{x}[\mathbf{j}])^2 \quad (24)$$

$$\text{subject to: } 0 \leq y_k[\mathbf{i}] \leq 1, \forall \mathbf{i}, k$$

The mean-squared error criterion is a commonly used fidelity metric for signal recovery from nonuniform samples using iterative methods [Marvasti et al. 1991]. It has also been used to derive iterative methods for image super-resolution [Elad and Feuer 1997; Irani and Peleg 1990]. The optimization problem of Eq. (24) may be solved using an iterative algorithm that may be expressed entirely in terms of texture resampling operations. The optimal subframes are computed using the iterative gradient descent algorithm,

$$y_k^{(0)}[\mathbf{q}] = \sum_{\mathbf{j}} \rho_k(\mathbf{q}, \mathbf{j}) x[\mathbf{j}], \quad \forall k, \quad (25)$$

$$\hat{x}^{(n)}[\mathbf{j}] = \sum_k \sum_{\mathbf{i}} \rho_k(\mathbf{i}, \mathbf{j}) y_k^{(n)}[\mathbf{i}], \quad (26)$$

$$\frac{\partial J}{\partial y_k^{(n)}[\mathbf{q}]} = - \sum_{\mathbf{j}} \rho_k(\mathbf{q}, \mathbf{j}) (x[\mathbf{j}] - \hat{x}^{(n)}[\mathbf{j}]), \quad (27)$$

$$y_k^{(n+1)}[\mathbf{q}] = \psi \left( y_k^{(n)}[\mathbf{q}] - \mu \frac{\partial J}{\partial y_k^{(n)}[\mathbf{q}]} \right), \quad \forall k, \quad (28)$$

$$\psi(a) = \begin{cases} a & a \in [0, 1] \\ 0 & a < 0 \\ 1 & a > 1 \end{cases}, \quad (29)$$

$$\{\mathbf{y}_k^*[\mathbf{q}]\} = \lim_{n \rightarrow \infty} \{y_k^{(n)}[\mathbf{q}]\}, \quad (30)$$

where  $\mu$  is a step-size parameter indicating the fraction of error to be incorporated at each iteration. Eq. (25) initializes the subframes. In general, we could also use any of the naïve subframe generation methods described in Section 3.3 to initialize the subframes. The preceding algorithm consists of two passes: In the forward pass (i.e., modeling pass), we compute  $\hat{x}^{(n)}[\mathbf{j}]$  from the current guesses of the subframes  $y_k^{(n)}[\mathbf{i}]$  using (26). A backward pass (i.e., error correction pass) then updates the subframes based on prediction errors using (27) and (28). This algorithm may be intuitively understood as an iterative process of computing an error in the reference high-resolution coordinate system and projecting a filtered version of it back onto the subframe data, to form better estimates of the subframes. The subframe clipping of Eq. (29) ensures that physical range limits of the display are not exceeded. Since the problem is convex with convex constraints, this process is guaranteed to converge to the optimal solution.

The filters  $\rho_k(\mathbf{i}, \mathbf{j})$  are anisotropic and space varying in general. To compute  $\rho_k(\mathbf{i}, \mathbf{j})$  in practice, we approximate the integral of Eq. (5) by discrete sums as

$$\rho_k(\mathbf{i}, \mathbf{j}) = \sum_{\mathbf{n}=(-M, -M)}^{(+M, +M)} p(\mathbf{n} L) r(\mathbf{m}_k^{-1}(\mathbf{j} - \mathbf{n} L) - \mathbf{i}), \quad (31)$$

$$= \sum_{\mathbf{n}=(-M, -M)}^{(+M, +M)} p(\mathbf{j} - \mathbf{m}_k(\mathbf{i} + \mathbf{n} L)) r(\mathbf{n} L) |[\mathbf{J}_k]_{\mathbf{i}}|, \quad (32)$$

where  $L$  is the discretization period and  $[\mathbf{J}_k]_{\mathbf{i}}$  is the Jacobian of warp  $\mathbf{m}_k$  evaluated at  $\mathbf{i}$ . We use Eq. (31) to compute the filter coefficients needed to produce an output at location  $\mathbf{j}$  by filtering a neighborhood  $\mathbf{i} \in \mathcal{N}(\mathbf{m}_k^{-1}(\mathbf{j}))$ . We use Eq. (32) to compute the filter coefficients

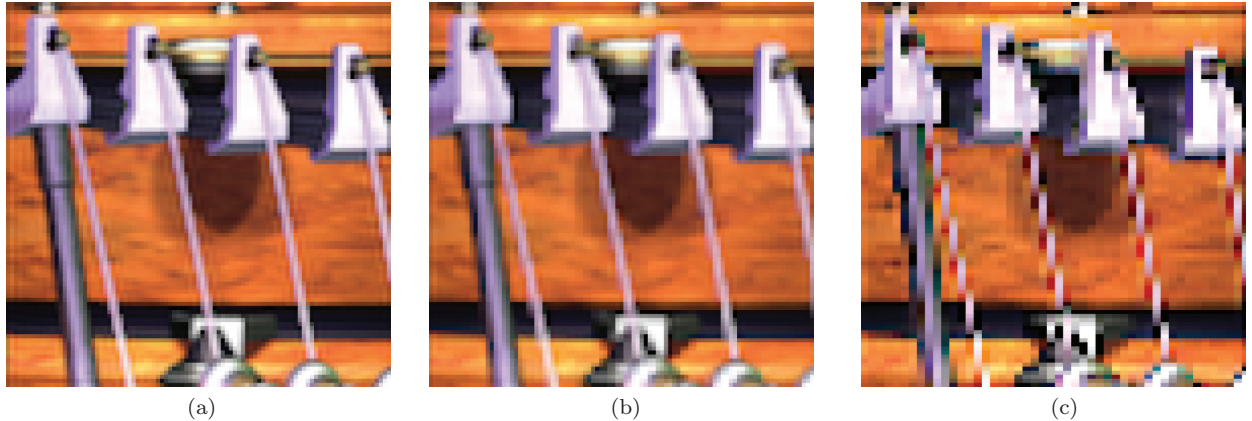


Fig. 15. Result of optimal subframe generation in the case of critical uniform and recurrent nonuniform display supersampling: (a) critical uniform DSS; (b) optimal recurrent nonuniform DSS; (c) a representative aliased subframe.

needed to produce an output at location  $\mathbf{i}$  by filtering a neighborhood  $\mathbf{j} \in \mathcal{N}(\mathbf{m}_k(\mathbf{i}))$ . Thus, one set of filter coefficients is used for the forward pass and another set for the backward error correction pass.

Figure 15(a) and 15(b) shows the result of superimposed rendering four low-resolution subframes with the relative sampling geometry of Figures 3(a) and 3(b), respectively, using the optimal iterative subframe generation approach. An example subframe shown in Figure 15(c) illustrates that the subframes are indeed aliased, while the superimposed output is a high-quality, sharp, yet alias-free rendering of the original image. The results may be compared with those obtained with the naïve approaches presented in Section 3.3. It should be noted that the iterative algorithm is equally applicable to the general nonuniform sampling case (examples are provided in Section 6).

## 5.2 Fast Filter Bank Subframe Generation

The previous iterative algorithm produces optimal subframes for an arbitrary number of component subframes. It is worth noting that it does, however, require access to all subframes to compute the model prediction  $\hat{x}^{(n)}[\mathbf{j}]$  in Eq. (26). For systems without shared memory, the algorithm may be unsuitable for scalable real-time implementation, since each computation module must redundantly compute the entire forward pass before it can derive its subframes. This bottleneck only becomes worse as the number of subframes is increased. Further, even if shared memory is available, performing more than one or two iterations of the algorithm would be computationally infeasible in real time.

In this section, we derive an efficient noniterative algorithm for subframe generation that may be implemented as a bank of filters operating directly on the input image to be displayed. This is motivated by our analysis of Section 4 that proved that even when the resulting display sampling is nonuniform, a bank of analysis filters may cancel aliasing. The optimal filters are derived by directly finding the impulse response (possibly space varying) of a linear approximation to the nonlinear optimal iterative algorithm of Section 5.1. The linear system approximation to the nonlinear iterative algorithm of (25) through (30) is made by simply eliminating the nonlinear clipping operation of Eq. (29). This step results in three cases discussed in the following subsections.

### 5.2.1 Subframe Generation for General Sampling Geometries.

General nonuniform supersampling is the broadest case to consider.

It commonly occurs when multiple commodity projectors are superimposed and their respective geometric warps (typically, planar perspective transformations or homographies) result in a spatially varying nonuniform grid. We present the following theorem and algorithm for this case. Further discussion on practical implementations and resulting performance may be found in Section 6.

**THEOREM 5.1.** *In the case of general nonuniform display supersampling with  $N$  superimposed subframes,  $\exists$  space-varying filters  $\phi_k(\mathbf{i}, \mathbf{j})$ ,  $k = 0, 1, \dots, N - 1$  such that the equation*

$$y_k[\mathbf{i}] = \sum_{\mathbf{j}} \phi_k(\mathbf{i}, \mathbf{j}) x[\mathbf{j}] \quad (33)$$

*produces the same subframes as the iterative algorithm of (25) through (30) when  $\psi(a) \doteq a$ .*

**PROOF.** Since the iterative algorithm is now linear, it may be characterized by a spatially varying impulse response.  $\square$

The subframe generation may be accomplished by a bank of  $N$  space-varying filters, each operating on the high-resolution image to produce component subframes. This means that for each low-resolution subframe pixel to be rendered, there is potentially a different filter that operates on high-resolution pixels in the neighborhood around the warped pixel-center. To find the filter coefficients for the  $k$ th subframe that filter  $\mathbf{j} \in \mathcal{N}(\mathbf{m}_k(\mathbf{i}))$  for a given  $\mathbf{i}$ , we evaluate the response at  $\mathbf{i}$  of the  $k$ th subframe to the linearized iterative algorithm driven with impulse inputs. Successively measuring the responses at  $\mathbf{i}$  to single impulses at various locations  $\mathbf{j}$  is too time consuming to be practical. Instead, we evaluate subframe responses at multiple subframe pixels in parallel by restricting the neighborhoods to a finite  $W \times W$  window while spacing impulses apart by  $W$ . Thus, only  $W^2$  impulse training images are needed to cover all the locations of  $\mathcal{N}(\mathbf{m}_k(\mathbf{i}))$ . This spacing also eliminates spurious aliasing due to multiple impulses contributing to a single observed response at a time. The  $W \times W$  filter coefficients  $h_{k,i}[\mathbf{w}]$  are given by

$$h_{k,i}[\mathbf{w}_{t,k,i}] = y_k[\mathbf{i}], \quad \forall t, \quad (34)$$

where  $\mathbf{w}_{t,k,i}$  represents the location of an impulse in the  $W \times W$  neighborhood  $\mathcal{N}(\mathbf{m}_k(\mathbf{i}))$  for the  $t$ th impulse training image. Since there are  $W^2$  training images, each image determines a unique filter

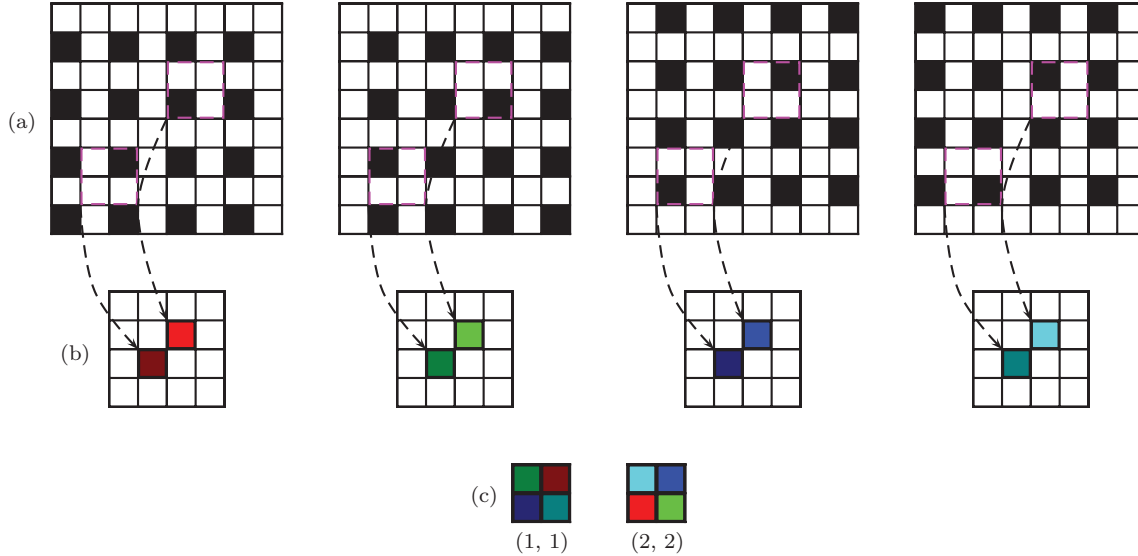


Fig. 16. Deriving component filters for general nonuniform sampling geometries. This example illustrates the filter coefficient generation process for a  $2 \times 2$  filter neighborhood for convenience. (a) High-resolution impulse training images with impulses shown in black. (b) Result of linearized iterative algorithm for two different subframe pixels at pixel locations (1,1) and (2,2). Each unique color indicates a different pixel intensity. (c) Resulting per-pixel  $2 \times 2$  filter coefficients. In this case, one set of filter coefficients per subframe pixel is needed since the subframe generation filter bank is space varying.

coefficient of  $h_{k,i}[\mathbf{w}]$ . Once computed, the filter may be used to compute the response  $y_k[\mathbf{i}]$  to an arbitrary input using the equation

$$y_k[\mathbf{i}] = \sum_{\mathbf{w}} h_{k,i}[\mathbf{w}] x_i[\mathbf{w}], \quad (35)$$

where  $x_i[\mathbf{w}]$  represents the  $W \times W$  neighborhood of  $x$  around  $\mathbf{m}_k(\mathbf{i})$ . Figure 16 illustrates the process to compute a  $2 \times 2$  filter for a specific subframe location of a component subframe. Example images using this technique are presented in Section 6.

One additional consideration is storing the space-varying filter coefficients, once computed. This may seem a daunting task requiring special parameterizations. However, if commodity graphics hardware is used for the rendering, the required texture memory is readily available.

**5.2.2 Subframe Generation for Affine Warps.** We can simplify the previous result in the case of affine warping. Recurrent nonuniform sampling is simply a special case of affine warps when the warps are represented by shifts.

**THEOREM 5.2.** *In the case of display supersampling with  $N$  superimposed subframes where geometric mappings  $\mathbf{m}_k$  are all affine,  $\exists$  filters  $\phi_k(\mathbf{i}, \mathbf{j}) = \phi'_k(\mathbf{j} - \mathbf{m}_k(\mathbf{i}))$ ,  $k = 0, 1, \dots, N-1$  such that the equation*

$$y_k[\mathbf{i}] = \sum_{\mathbf{j}} \phi'_k(\mathbf{j} - \mathbf{m}_k(\mathbf{i})) x[\mathbf{j}] \quad (36)$$

*produces the same subframes as the iterative algorithm of (25) through (30) with  $\psi(a) \doteq a$ .*

This result is proved in the Appendix. This theorem means  $\phi_k(\mathbf{m}_k^{-1}(\mathbf{i}), \mathbf{j})$  is spatially invariant. Thus, when the warps are affine, the linearized iterative algorithm is equivalent to a subframe generation filter bank of  $N$  linear space-invariant filters  $\phi'_k$ , each operating on the high-resolution image to produce component subframes.

To get the impulse responses in this case, we need to evaluate the subframe responses to all impulses at locations  $\mathbf{j} \in \mathcal{N}(\mathbf{m}_k(\mathbf{i}))$ .

that contribute to a single output pixel at  $y_k(\mathbf{i})$ . In this case, it is sufficient to evaluate the response at any  $\mathbf{i}$  for each  $k$ . The  $W \times W$  filter coefficients  $h_k[\mathbf{w}]$  are given by

$$h_k[\mathbf{w}_{t,k}] = y_k[\mathbf{i}], \quad \forall t, \quad (37)$$

where  $\mathbf{w}_{t,k}$  represents the location of an impulse in the  $W \times W$  neighborhood  $\mathcal{N}(\mathbf{m}_k(\mathbf{i}))$  for the  $t$ th impulse training image and any  $\mathbf{i}$ . As before, each of the  $W^2$  training images determines a unique filter coefficient of  $h_k[\mathbf{w}]$ . The resulting filter leads to the response  $y_k[\mathbf{i}]$  to an arbitrary input using the equation

$$y_k[\mathbf{i}] = \sum_{\mathbf{w}} h_k[\mathbf{w}] x_i[\mathbf{w}], \quad (38)$$

where  $x_i[\mathbf{w}]$  represents the  $W \times W$  neighborhood of  $x$  around  $\mathbf{m}_k(\mathbf{i})$ . Figure 17 illustrates the process to compute a  $2 \times 2$  filter for one of the component subframes.

It is worthwhile to examine these filters more closely. Figure 18 shows the frequency responses of the optimal DSS anti-aliasing filters in the case of the recurrent nonuniform sampling geometry given in Figure 3(b). The complementary nature of these filters is clear from their frequency responses. The corresponding result and subframe (see Figures 19(a) and 19(b)) are comparable in image quality to the results of the optimal nonlinear iterative algorithm (recall Figures 15(b) and 15(c), respectively) with a much more efficient implementation.

**5.2.3 Subframe Generation for Uniform Critically Sampled Geometries.** The case of uniform critical sampling was analyzed by Said [2006], who showed that the optimal solution for the subframes (ignoring signal range limits) could be derived from a linear shift-invariant filtering of  $x[\mathbf{j}]$ . In our case, the equivalent shift-invariant inverse filter may therefore be obtained as the impulse response of the linearized iterative algorithm. We create an impulse training

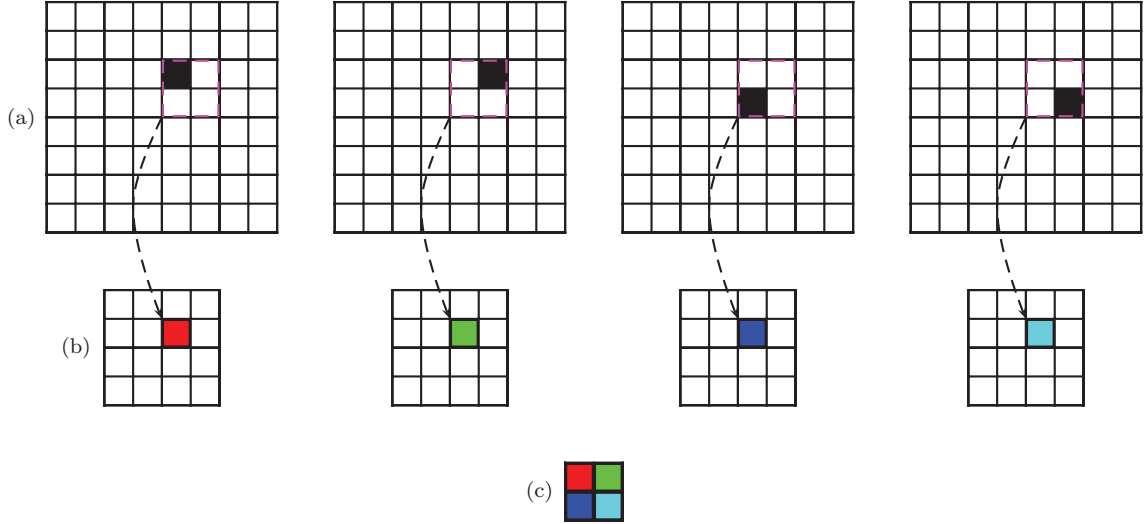


Fig. 17. Deriving component filters for recurrent nonuniform sampling geometries. This example illustrates the filter coefficient generation process for a  $2 \times 2$  filter neighborhood for convenience. (a) High-resolution impulse training images with impulses shown in black. (b) Result of linearized iterative algorithm for a particular subframe pixel. Each unique color indicates a different pixel intensity. (c) Resulting  $2 \times 2$  filter coefficients. In this case, only one set of filter coefficients per component subframe suffices to filter all the high-resolution neighborhoods corresponding to any subframe pixel.

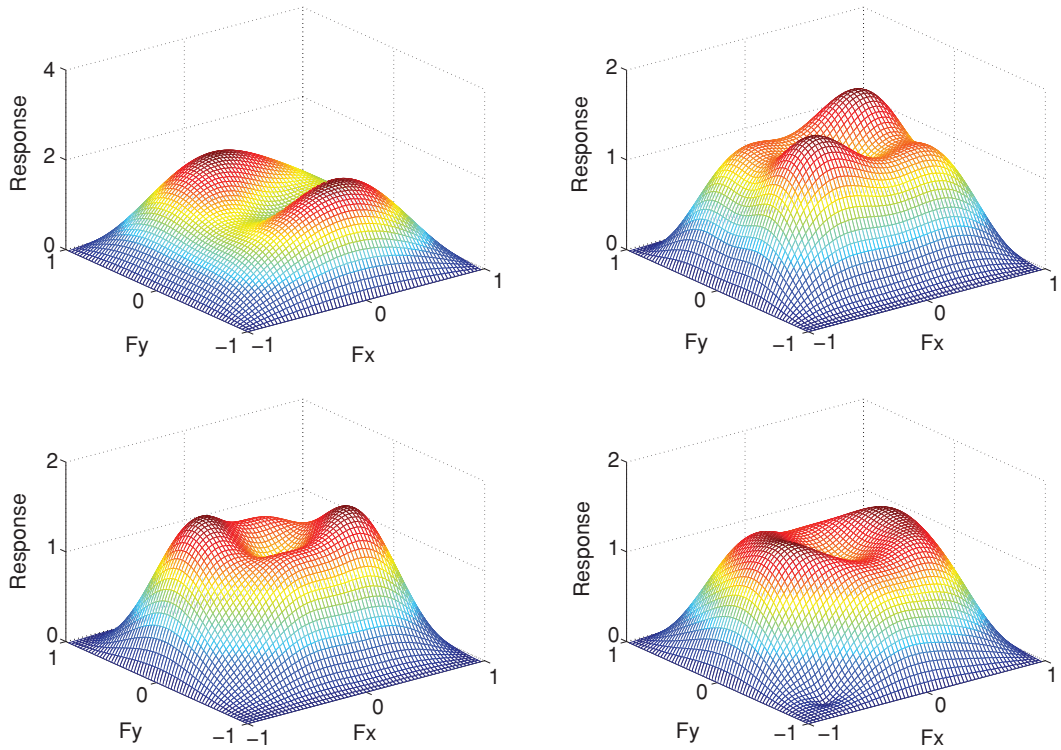


Fig. 18. Frequency responses of the four component filters in the alias-cancellation recurrent nonuniform filter bank. Their complementary nature should be readily apparent.

image with an impulse at its center and go through several iterations of the iterative algorithm. The impulse response is simply read from the nonzero values of  $y_k^{(n)}[i]$  after  $n$  iterations. Figure 20(a) shows the frequency response of the optimal inverse filter; it is immediately

clear that it is a deblurring filter. Figure 20(b) illustrates the performance of the approximate filters. These results compare favorably with those obtained by the optimal nonlinear iterative algorithm (recall Figure 15(a)).

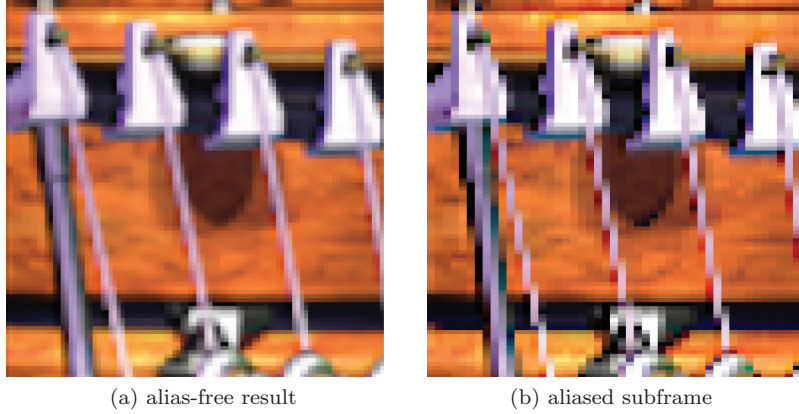


Fig. 19. Performance of fast subframe generation filter bank for the recurrent nonuniform supersampling geometry of Figure 3(b). These results achieve similar image quality to their slower-to-compute counterparts in Figures 15(b) and 15(c), respectively.

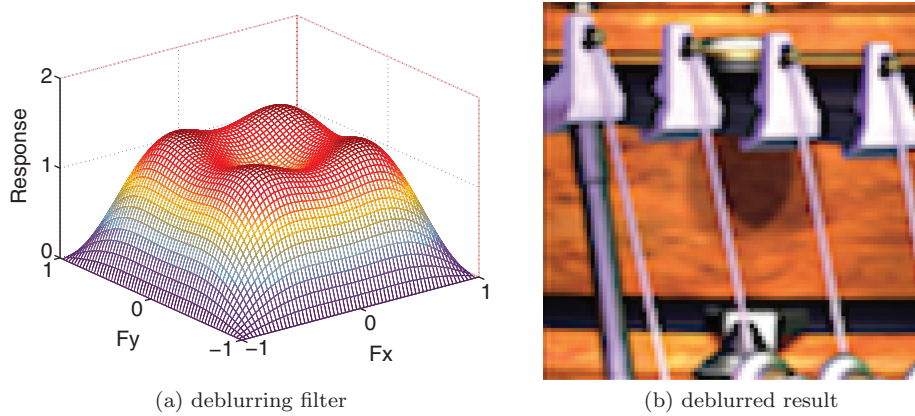


Fig. 20. Performance of fast subframe generation filter bank for the critical uniform supersampling geometry of Figure 3(a). The filter bank reduces to a single shift-invariant deblurring filter. The resulting image quality is similar to that derived using slower optimal iterative algorithm in Figure 15(a).

## 6. REAL-TIME DISPLAY SUPERSAMPLING

To validate the fundamental theory of display supersampling, we demonstrate in this section experimental results on prototype real-time superimposed display systems and discuss issues to consider with such practical systems. The systems consist of substantially overlapping multiple “low-resolution”  $1024 \times 768$  projectors and displaying higher-resolution content (between  $1.25 \times$  and  $2 \times$  higher, typically  $1920 \times 1080$ ) on them. A workstation fitted with multiple commodity graphics cards (nVidia GeForce 8800 GTX) computes the optimal subframes and drives the projectors. Figures 21(a) and 21(b) show prototype 4-projector and 10-projector systems, respectively. For the discussion, it is assumed that the projectors output onto a planar screen surface. Also, the projectors’ frame buffers are considered to be the aforementioned subframes.

The analysis in Section 3.2 assumes known warps  $\mathbf{m}_k(\cdot)$  between each projector and the reference coordinate system. In a practical situation, however, the projectors are likely to be geometrically misaligned with respect to one another due to their different optical paths and physical placement. Further, the superimposed grid is almost always the general nonuniform sampling case shown in

Figure 3(c). We introduce a camera into the setup to perform a one-time calibration procedure. An efficient 2D structured-light coding technique [Chang 2003] is used to automatically compute the projector-camera mapping at every subframe location. The technique is robust and generates a dense subpixel mapping between projector pixels and camera pixels, regardless of geometry [Chang 2004]. For simplification, each mapping is further reduced to a  $3 \times 3$  homography using least squares over the dense set of correspondence pairs. Additionally, the camera may be used to estimate other differences among the projectors (e.g., color, luminance, black offset, etc.); these additions are described in Damera-Venkata and Chang [2007b]. After the reference coordinate system is selected or else computed with respect to the camera coordinate system, we finally obtain the desired mappings from each projector to the reference coordinate system. These mappings are almost always spatially varying and result in the general nonuniform supersampling case.

With regard to efficient implementation, the fast iterative algorithm from Section 5.2.1 is used to train and compute appropriate space-varying filters at every projector pixel location. A neighborhood of  $4 \times 4$  is considered for a total of 16 impulse training images. Because of the filtering nature of the algorithm, it is efficiently

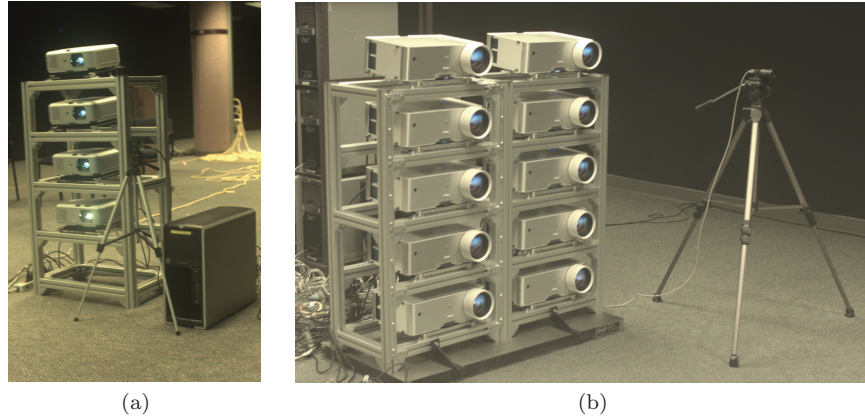


Fig. 21. Prototype supersampled displays with: (a) four-; and (b) ten-superimposed projectors.

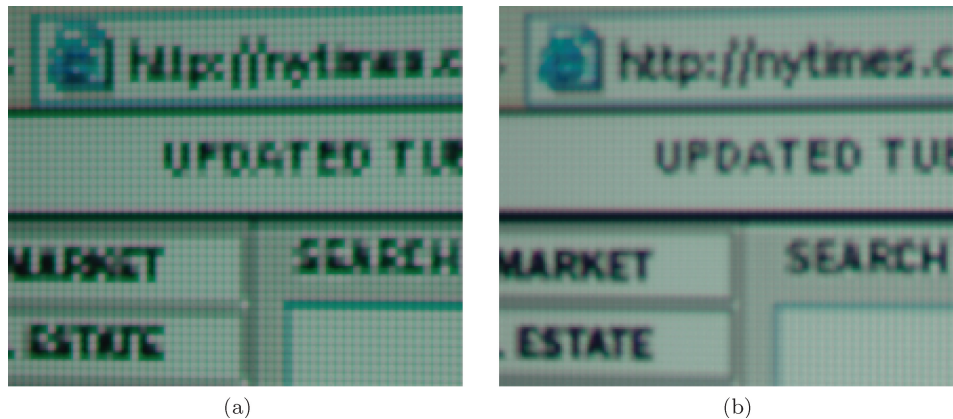


Fig. 22. Experimental results for four superimposed projectors with DSS: (a) one projector subframe; (b) superimposing all four projectors' subframes. Note how the higher frequency of the content and the text resolvability increase dramatically as subframes are added.

implemented on the pixel shaders of the graphics processing unit (GPU) of commodity graphics cards. It should be emphasized that the construction of these space-varying filters depends only on the geometric warps and not on the actual content to be displayed.

Finally, we need to consider the real-time application of these filters to generate the final displayed output. For a given high-resolution input image, projector  $k$ 's subframe  $y_k[i]$  is simply constructed by using Eq. (35) in Section 5.2.1. With this construction, the subframes may be efficiently computed in parallel and at fast frame rates on commodity GPU pixel shaders.

Figure 22 shows an actual captured image of the four-projector superimposed display. The desired image is higher resolution than any of the component projectors (in this case,  $1.5625 \times$  higher). The subframes of every projector are computed in real time for each input image; Figure 22(a) shows a typical single subframe possessing significant aliasing.<sup>4</sup> Superimposing all four subframes leads to a dramatic enhancement in resolution and resolvability with DSS (Figure 22(b)); in particular, consider the improvement with the words “nytimes” and “ESTATE.” As seen in the figure, the screen-

door artifact from typical projectors is mitigated considerably. Of course, the superimposed display naturally becomes brighter with the addition of each projector, demonstrating a display with enhanced resolution as well as increased brightness. Similar improvements can be seen in Figure 23. It should be clear that using DSS we can achieve much better text and line resolvability.

Even more dramatic results can be seen for a ten-projector system, shown in Figure 24. In this case the desired image is  $1.875 \times$  greater in resolution than any of the component projectors. In addition to the inherent  $10 \times$  brightness gain (not shown), the resulting image from superimposing ten projectors results in considerably more detail with the wires and the bottom pegs in the image.

These examples highlight the feasibility and key advantages of practical display supersampling. The prototype systems can perform very efficiently using commodity GPU hardware. With the camera-based technique, geometric mappings are automatically computed in less than eight seconds per projector. It should be emphasized that the theory applies to generalized projector warps and display surfaces, not just to homographies. The four projectors' subframes are all generated at real-time rendering rates of 60 frames per second, independent of the content dimensions. In contrast to prior work [Jaynes and Ramakrishnan 2003], we believe our prototype systems are the first superimposed displays that demonstrate super-resolution for arbitrary nonuniform sampling and at real-time rates.

<sup>4</sup>The brightness of the single-projector images in this section have been enhanced to facilitate a better comparison against the multiprojector result. In actuality, these single-projector images are considerably dimmer than their multiprojector counterparts.

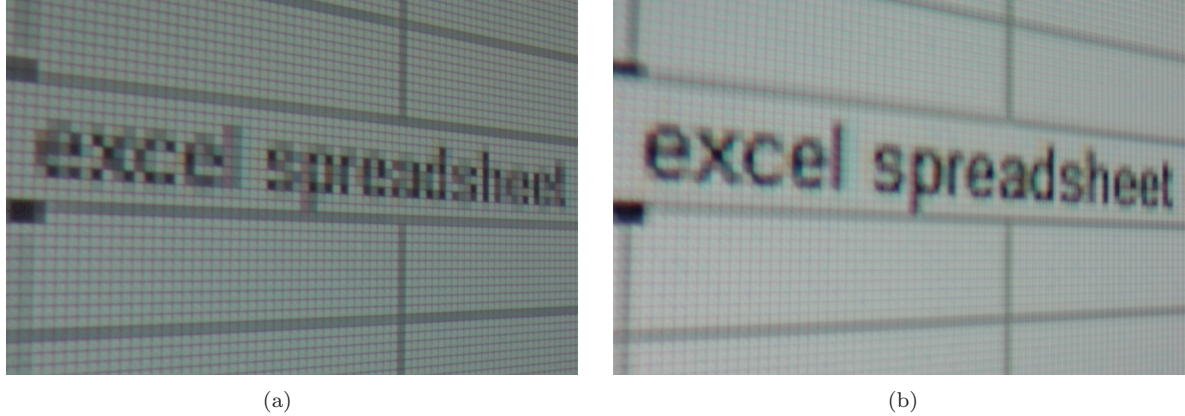


Fig. 23. Experimental results for four superimposed projectors with DSS: (a) one projector subframe; (b) superimposing all four projectors' subframes. Note how the higher frequency of the content and the text resolvability increases dramatically as subframes are added.

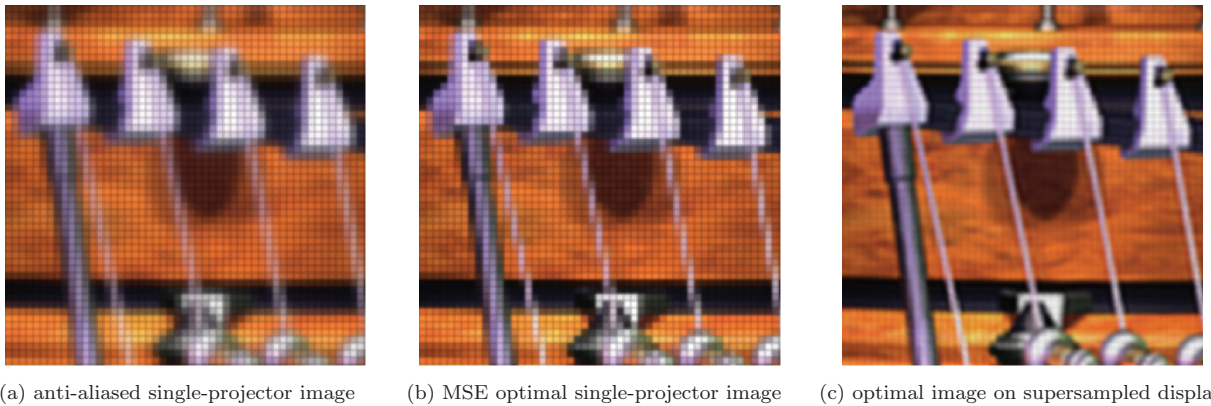


Fig. 24. Comparison of the image quality of a single-projector display versus a supersampled high-brightness multiprojector display formed by superimposing ten commodity projectors. A single projector must: (a) blur a high-resolution input to prevent aliasing; or (b) alias in order to display high frequencies. (c) With proper subframe generation from Section 5.2.1 to compensate for the effects of nonuniform supersampling, an alias-free high-resolution image may be rendered.

## 7. CONCLUSION

We have developed fundamental theory governing the display of high-quality, anti-aliased images on supersampled displays. We have also described both optimal and practical approaches to image rendering and described real implementations on commodity graphics hardware. Key contributions of this article include:

- (1) an analysis of display supersampling, demonstrating the underlying mechanism of resolution enhancement and the effects of sampling configuration, sampling density, and pixel reconstruction functions;
- (2) proof that super-Nyquist rendering is indeed possible on supersampled displays, even for nonuniform sampling;
- (3) a novel and nontrivial alias-cancellation (filter bank) view of optimal rendering;
- (4) an understanding of the limits to resolution achievable resolution gain;
- (5) practical and efficient methods to achieve high-quality, real-time display supersampling via superimposed projection; and
- (6) a view of the optimal rendering task in relation to classical problems in signal processing, computer graphics, and computer vision.

Due to the close relation of this problem to anti-aliasing and texture mapping in computer graphics and super-resolution in computer vision, some of the ideas presented in this work may be leveraged in these domains also. While this article has focused on DSS via the superimposition of multiple superimposed subframes, more general ways of combining display samples also could be analyzed in this framework.

## A. APPENDIX

### A.1 Proof of Theorem 4.1

The proof is based on Eldar and Oppenheim's [2000] filter bank interpretation of the generalized sampling theorem of Yao and Thomas [1967] for the case of recurrent nonuniform sampling. Figure 25 shows the filter bank representation of their sampling theorem in the case of generalized reconstruction from two recurrent samples per sampling period. The average sampling period in this case is equal to the Nyquist period  $T$ . The analysis bank (signal sampling) in their problem is defined while the reconstruction filters  $g_k(t)$  are free parameters to be chosen. On the other hand, in the case of display supersampling, the synthesis bank (reconstruction bank) is determined by the geometry, whereas the filters of the analysis

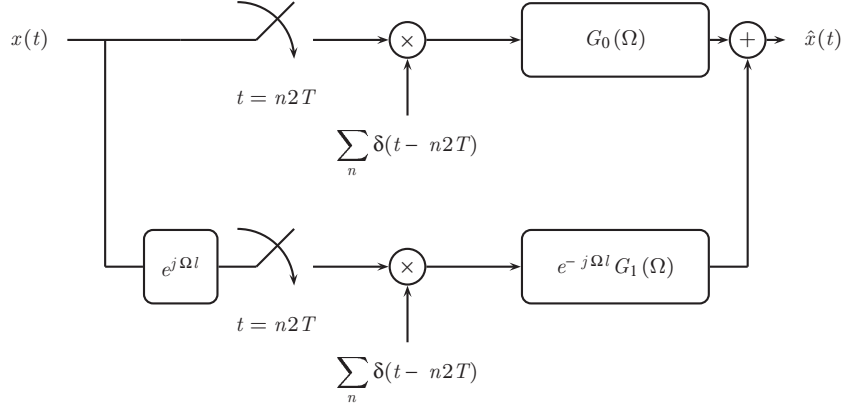


Fig. 25. Generalized sampling theorem showing reconstruction from recurrent nonuniform samples of a signal. The analysis bank shows samples drawn at period  $2T$  with relative nonuniform offset  $l$ . This is a dual of DSS where we are free to choose synthesis filters while the analysis filters are determined by the sampling geometry.

bank  $h_k(t)$  are the free parameters to be chosen. Thus, the alias-cancellation problem in DSS is the dual of the problem of signal recovery from generalized samples. To relate the two cases, we call on the following lemma, which is a standard result in the theory of filter banks [Strang and Nguyen 1996].

**LEMMA A.0.1.** *In a perfect reconstruction filter bank, the analysis and synthesis filters may be swapped without affecting the perfect reconstruction property.*

We apply Lemma A.0.1 to Figure 25. Without loss of generality this may be seen in the two-subframe case by comparing the filter banks of Figure 25 and Figure 8. The analysis and synthesis filters (denoted by  $\check{H}_k$  and  $\check{G}_k$ , respectively) in the case of Figure 25 are

$$\check{H}_0(\Omega) = 1, \quad \check{H}_1(\Omega) = e^{j\Omega l}, \quad \check{G}_0(\Omega) = 1, \quad \check{G}_1(\Omega) = e^{-j\Omega l} G_1(\Omega).$$

The analysis and synthesis filters (denoted by  $\check{H}_k$  and  $\check{G}_k$ , respectively) in the case of Figure 8 are

$$\check{H}_0(\Omega) = 1, \quad \check{H}_1(\Omega) = e^{j\Omega l} H_1(\Omega), \quad \check{G}_0(\Omega) = 1, \quad \check{G}_1(\Omega) = e^{-j\Omega l}.$$

We see that the two banks indeed have their analysis and synthesis filters swapped, except for the sign of the shift  $l$  in the exponent. This is easily remedied by allowing a negative  $l$  in the bank of Figure 25. This means that the optimal subframe generation filters are just the synthesis filters of Figure 25 with the sign of the samples reversed. This is equivalent to swapping the analysis and synthesis banks and reversing the ordering. Thus, we obtain the optimal subframe generation filter coefficients of Theorem 4.1.  $\square$

## A.2 Proof of Theorem 5.2

The proof is by induction. First note that when  $\mathbf{m}_k$  are affine,  $\rho_k(\mathbf{i}, \mathbf{j}) = \rho'_k(\mathbf{m}_k^{-1}(\mathbf{j}) - \mathbf{i}) = \rho''_k(\mathbf{j} - \mathbf{m}_k(\mathbf{i}))$ . The first equality was shown by Heckbert [1989] by imposing the affine condition on Eq. (6). The second equality may be shown by similarly imposing the affine condition on Eq. (5). Hence, the initial guess of Eq. (25) satisfies the theorem. Assume that the result of  $n$  iterations of the linearized algorithm can be represented by the filter  $\theta_k(\mathbf{j} - \mathbf{m}_k(\mathbf{i}))$ . The result of the iteration  $n + 1$  may be written as

$$\hat{x}^{(n)}[\mathbf{j}] = \sum_k \sum_{\mathbf{i}} \rho'_k(\mathbf{m}_k^{-1}(\mathbf{j}) - \mathbf{i}) y_k^{(n)}[\mathbf{i}]. \quad (39)$$

$$\frac{\partial J}{\partial y_p^{(n)}[\mathbf{q}]} = - \sum_{\mathbf{j}} \rho''_p(\mathbf{j} - \mathbf{m}_p(\mathbf{q})) (x[\mathbf{j}] - \hat{x}^{(n)}[\mathbf{j}]). \quad (40)$$

$$y_p^{(n+1)}[\mathbf{q}] = \sum_{\mathbf{j}} \theta_p(\mathbf{j} - \mathbf{m}_p(\mathbf{q})) x[\mathbf{j}] - \mu \frac{\partial J}{\partial y_p^{(n)}[\mathbf{q}]}, \quad \forall p. \quad (41)$$

Expanding the term  $\sum_{\mathbf{j}} \rho''_p(\mathbf{j} - \mathbf{m}_p(\mathbf{q})) \hat{x}^{(n)}[\mathbf{j}]$  from Eq. (40), we have

$$\begin{aligned} & \sum_{\mathbf{j}} \rho''_p(\mathbf{j} - \mathbf{m}_p(\mathbf{q})) \sum_k \sum_{\mathbf{i}} \rho'_k(\mathbf{m}_k^{-1}(\mathbf{j}) - \mathbf{i}) \sum_{\mathbf{l}} \theta_k(\mathbf{l} - \mathbf{m}_k(\mathbf{i})) x[\mathbf{l}] \\ &= \sum_{\mathbf{l}} \underbrace{\sum_{k, \mathbf{j}, \mathbf{i}} \rho''_p(\mathbf{j} - \mathbf{m}_p(\mathbf{q})) \rho'_k(\mathbf{m}_k^{-1}(\mathbf{j}) - \mathbf{i}) \theta_k(\mathbf{l} - \mathbf{m}_k(\mathbf{i}))}_{\zeta(\mathbf{q}, \mathbf{l})} x[\mathbf{l}] . \end{aligned} \quad (42)$$

Note that  $\zeta(\mathbf{m}_p^{-1}(\mathbf{q} - \mathbf{t}), \mathbf{l} - \mathbf{t})$

$$\begin{aligned} &= \sum_{k, \mathbf{j}, \mathbf{i}} \rho''_p(\mathbf{j} - \mathbf{q} + \mathbf{t}) \rho'_k(\mathbf{m}_k^{-1}(\mathbf{j}) - \mathbf{i}) \theta_k(\mathbf{l} - \mathbf{t} - \mathbf{m}_k(\mathbf{i})) \\ &= \sum_{k, \mathbf{j}', \mathbf{i}'} \rho''_p(\mathbf{j}' - \mathbf{q}) \rho'_k(\underbrace{\mathbf{m}_k^{-1}(\mathbf{j}' - \mathbf{t}) - \mathbf{i}' + \mathbf{m}_k^{-1}(\mathbf{t})}_{\mathbf{m}_k^{-1}(\mathbf{j}') - \mathbf{i}'} \theta_k(\mathbf{l} - \mathbf{m}_k(\mathbf{i}')) \\ &= \zeta(\mathbf{m}_p^{-1}(\mathbf{q}), \mathbf{l}) \end{aligned} \quad (43)$$

since for affine  $\mathbf{m}_k$ ,  $\mathbf{m}_k^{-1}(\mathbf{x} - \mathbf{y}) = \mathbf{m}_k^{-1}(\mathbf{x}) - \mathbf{m}_k^{-1}(\mathbf{y})$ . This implies that  $\sum_{\mathbf{j}} \rho''_p(\mathbf{j} - \mathbf{m}_p(\mathbf{q})) \hat{x}^{(n)}[\mathbf{j}] = \sum_{\mathbf{j}} \zeta(\mathbf{q}, \mathbf{j}) x[\mathbf{j}] = \sum_{\mathbf{j}} \eta_p(\mathbf{j} - \mathbf{m}_p(\mathbf{q})) x[\mathbf{j}]$  for some  $\eta_p(\cdot)$ .

Substituting into Eq. (41), we have

$$\begin{aligned} y_p^{(n+1)}[\mathbf{q}] &= \sum_{\mathbf{j}} (\theta_p + \mu \rho''_p - \mu \eta_p)(\mathbf{j} - \mathbf{m}_p(\mathbf{q})) x[\mathbf{j}] \\ &= \sum_{\mathbf{j}} \phi_p(\mathbf{j} - \mathbf{m}_p(\mathbf{q})) x[\mathbf{j}]. \end{aligned} \quad (44)$$

This completes the proof.  $\square$

## ACKNOWLEDGMENTS

The authors would like to thank A. Paruchuri for his GPU expertise and invaluable help with implementing the prototype real-time supersampled displays. They would also like to acknowledge R. Ulichney for his help in generating some of the included results.

## REFERENCES

- AKENINE-MÖLLER, T. AND HAINES, E. 2002. *Real-Time Rendering*. A. K. Peters Ltd., Natick, MA.
- ALLEN, W. AND Ulichney, R. 2005. Wobulation: Doubling the addressed resolution of projection displays. In *Proceedings of the SID Symposium Digest of Technical Papers (SID)*. Boston, MA, 1514–1517.
- BAKER, S. AND KANADE, T. 2002. Limits on super-resolution and how to break them. *IEEE Trans. Pattern Anal. Mach. Intell.* 24, 1167–1183.
- BEN-EZRA, M., ZOMET, A., AND NAYAR, S. 2004. Jitter camera: High resolution video from a low resolution detector. In *Proceedings of the IEEE Conference on Computer Vision and Pattern Recognition (CVPR)*, 135–142.
- BROWN, M., MAJUMDER, A., AND YANG, R. 2005. Camera-Based calibration techniques for seamless multiprojector displays. *IEEE Trans. Visual. Comput. Graphics* 11, 193–206.
- CHANG, N. L. 2003. Efficient dense correspondences using temporally encoded light patterns. In *Proceedings of the IEEE International Workshop on Projector-Camera Systems (ProCams)*.
- CHANG, N. L. 2004. Creating interactive 3-D media with projector-camera system. In *Proceedings of the SPIE Visual Communications and Image Processing Conference (VCIP)*, vol. 5308, 850–861.
- COOK, R. 1986. Stochastic sampling in computer graphics. *ACM Trans. Comput. Graphics* 5, 51–72.
- CROW, F. 1981. A comparison of antialiasing techniques. *IEEE Comput. Graphics Appl.* 1, 40–48.
- DAMERA-VENKATA, N. AND CHANG, N. L. 2007a. On the resolution limits of superimposed projection. In *Proceedings of the IEEE International Conference on Image Processing (ICIP)*, vol. V, 373–376.
- DAMERA-VENKATA, N. AND CHANG, N. L. 2007b. Realizing super-resolution with superimposed projection. In *Proceedings of the IEEE International Workshop on Projector-Camera Systems (ProCams)*.
- DAMERA-VENKATA, N., CHANG, N. L., AND DiCARLO, J. M. 2007. A unified paradigm for scalable multi-projector displays. *IEEE Trans. Visualiz. Comput. Graphics (Proceedings of the IEEE Visualization/Information Visualization Conference)* 13, 6, 1360–1367.
- DEERING, M., WINNER, S., SCHEDIWY, B., DOFFY, C., AND HUNT, N. 1988. The triangle processor and normal vector shader: A VLSI system for high performance graphics. In *Proceedings of SIGGRAPH Computer Graphics Conference*, 21–30.
- DIPPE, M. AND WOLD, E. 1985. Antialiasing through stochastic sampling. In *Proceedings of SIGGRAPH, Computer Graphics Conference*, 69–78.
- ELAD, M. AND FEUER, A. 1997. Restoration of single super-resolution image from several blurred, noisy and down-sampled measured images. *IEEE Trans. Image Process.* 6, 1646–1658.
- ELDAR, Y. AND OPPENHEIM, A. 2000. Filterbank reconstruction of band-limited signals from nonuniform and generalized samples. *IEEE Trans. Signal Process* 48, 2864–2875.
- FUCHS, H., GOLDFEATHER, J., HILLQUIST, J. P., SPACH, S., AUSTIN, J. D., BROOKS, F. P., EYLES, J. G., AND POULTON, J. 1985. Fast spheres, shadows, textures, transparencies, and image enhancements in pixel-planes. In *Proceedings of SIGGRAPH Computer Graphics Conference*, 111–120.
- HAEBERLI, P. AND AKELEY, K. 1990. The accumulation buffer: Hardware support for high-quality rendering. In *Proceedings of SIGGRAPH Computer Graphics Conference*, 309–318.
- HARVILLE, M., CULBERTSON, B., SOBEL, I., GELB, D., FITZHUGH, A., AND TANGUAY, D. 2006. Practical methods for geometric and photometric correction of tiled projector displays on curved surfaces. In *Proceedings of the IEEE International Workshop on Projector-Camera Systems (ProCams)*, 52–59.
- HECKBERT, P. 1986. A survey of texture mapping. *IEEE Comput. Graphics Appl.* 6, 56–67.
- HECKBERT, P. 1989. Fundamentals of texture mapping and image warping. M.S. thesis, The University of California at Berkeley, Berkeley, California.
- IRANI, M. AND PELEG, S. 1990. Super resolution from image sequences. In *Proceedings of the 10th International Conference on Pattern Recognition*, 115–120.
- JAYNES, C. AND RAMAKRISHNAN, D. 2003. Super-Resolution composition in multi-projector displays. In *Proceedings of the IEEE International Workshop on Projector-Camera Systems (ProCams)*.
- JIANG, Z., WONG, T., AND BAO, H. 2003. Practical super-resolution from dynamic video sequences. In *Proceedings of the IEEE Conference on Computer Vision and Pattern Recognition (CVPR)*, 549–554.
- LIN, H. AND SHUM, H. 2004. Fundamental limits of reconstruction-based superresolution algorithms under local translation. *IEEE Trans. Pattern Anal. Mach. Intell.* 26, 83–97.
- MAJUMDER, A. 2005. Is spatial super-resolution feasible using overlapping projectors? In *Proceedings of the IEEE International Conference on Acoustics, Speech, and Signal Processing (ICASSP)*, 209–212.
- MAJUMDER, A. AND STEVENS, R. 2005. Perceptual photometric seamlessness in tiled projection-based displays. *ACM Trans. Graphics* 24, 111–134.
- MARVASTI, F., ANALOUI, M., AND GAMSHADZAH, M. 1991. Recovery of signals from nonuniform samples using iterative methods. *IEEE Trans. Signal Process.* 39, 872–877.
- MITCHELL, D. 1987. Generating antialiased images at low sampling densities. *Comput. Graphics* 21, 65–72.
- OPPENHEIM, A. AND SCHAFER, R. 1989. *Discrete-Time Signal Processing*. Prentice-Hall, Englewood-Cliffs, NJ.
- PARK, S., PARK, M., AND KANG, M. 2003. Super-Resolution image reconstruction: A technical overview. *IEEE Signal Process. Mag.* 20, 21–36.
- RASKAR, R., BROWN, M. S., YANG, R., CHEN, W., WELCH, G., AND TOWLES, H. 1999. Multi-Projector displays using camera-based registration. In *Proceedings of the IEEE Visualization Conference*, 161–152.
- SAID, A. 2006. Analysis of subframe generation for superimposed images. In *Proceedings of the IEEE International Conference on Image Processing (ICIP)*, 401–404.
- STRANG, G. AND NGUYEN, T. 1996. *Wavelets and Filter Banks*. Wellesley-Cambridge, Cambridge, MA.
- SURATI, R. 1999. Scalable self-calibrating display technology for seamless large-scale displays. Ph.D. thesis, Massachusetts Institute of Technology, Cambridge, Massachusetts.
- WANG, L., KANG, S., SZELISKI, R., AND SHUM, H. 2001. Optimal texture map reconstruction from multiple views. In *Proceedings of the IEEE Conference on Computer Vision and Pattern Recognition (CVPR)*, 347–354.
- YAO, K. AND THOMAS, J. 1967. On some stability and interpolatory properties of non-uniform sampling expansions. *IEEE Trans. Circ. Theory* 14, 404–408.
- ZOMET, A., RAV-ACHA, A., AND PELEG, S. 2001. Robust super-resolution. In *Proceedings of the IEEE Conference on Computer Vision and Pattern Recognition (CVPR)*, 645–650.

Received February 2007; revised September 2008; accepted December 2008